PCCP

ROYAL SOCIETY OF CHEMISTRY

PAPER

View Article Online
View Journal

Check for updates

Cite this: DOI: 10.1039/d6cp01022a

$NaMgX_3$ (X = Cl, Br) for solid electrolyte interphases: atomistic insights into defects, surfaces and doping strategies

Yohandys A. Zulueta, [a] Bao-Ngan Nguyen-Ha [bc] and Minh Tho Nguyen *[bc]

Received 20th March 2026,
Accepted 22nd May 2026

DOI: 10.1039/d6cp01022a

rsc.li/pccp

Progress in metal-ion batteries depends on engineered solid electrolyte interphases with tunable defect chemistry and robust mechanics. In this work, atomistic simulations provide a quantitative comparison of the properties of $NaMgCl_3$ and $NaMgBr_3$ with direct relevance to solid electrolyte interphase design. The results confirm wide band gaps of 5.0 eV ($NaMgCl_3$) and 3.7 eV ($NaMgBr_3$), establishing both compounds as electronically insulating and mechanically stable and suitable for the electrolyte interphase. Br substitution expands the lattice and octahedral volumes and lengthens Mg–X bonds, producing a softer, more deformable bromide framework that opens conduction channels. Defect chemistry is governed by Na–X Schottky formation, Na^+ and Li^+ Frenkel disorder, and aliovalent substitution: divalent substitution at Na^+-sites is the most practical Na^+ vacancy source (in particular the Zn^{2+} dopant) and trivalent dopants bind strongly but require non-equilibrium incorporation. Bulk metrics show that the Br^- anion lowers migration barriers and raises the conductivity ($E_a \sim 0.75$ eV, 7.6×10^{-12} S cm^{-1} for $NaMgCl_3$; $E_a \sim 0.41$ eV, 2.1×10^{-6} S cm^{-1} for $NaMgBr_3$). Surface energetics are facet dependent: lowest-energy facets are $NaMgCl_3$ [(001), $\gamma \sim 0.29$ J m^{-2}] and $NaMgBr_3$ [(111, $\gamma \sim 0.15$ J m^{-2}], while (100) is high-energy ($\sim$4.0–5.0 J m^{-2}); high-energy facets give the lowest surface barriers (*e.g.*, $NaMgCl_3$ (100): $E_a \sim 0.06$ eV, $\sigma \sim 1.24 \times 10^{-1}$ S cm^{-1} and $NaMgBr_3$ (100): $E_a \sim 0.06$ eV, $\sigma \sim 1.19 \times 10^{-3}$ S cm^{-1}) whereas stable facets are far less conductive. These computed results provide predictions for experimental synthesis, facet engineering, and controlled doping to tune interphase performance and harness defect-driven reorganization for conductive SEI formation.

1. Introduction

The development of advanced battery materials has become a central focus in energy storage research, driven by the demand for higher energy density, improved safety, and longer cycle life. Cathode materials such as layered transition-metal oxides, polyanionic compounds, and alloy-based anodes have widely been investigated for their ability to reversibly host alkali ions while maintaining structural stability. For their part, solid electrolytes including sulfides, oxides, and more recently halide-based systems have emerged due to their high ionic conductivity and enhanced chemical stability compared to conventional liquid electrolytes.[1–10]

A rechargeable battery is typically composed of a cathode that serves as the source of alkali ions, an anode that acts as the host material for their reversible insertion and extraction, and an electrolyte that mediates ion transport between the two electrodes, with a separator included to prevent electronic contact while allowing ionic conduction.[1–10] During operation, the interphases between electrodes and electrolyte play a decisive role in determining the performance and stability, and at these boundaries a passivation layer known as the solid electrolyte interphase (SEI) is formed, which governs ionic selectivity, mechanical resilience, and coulombic efficiency, ultimately determining the durability and safety of the battery system (*cf.* Scheme 1).[1–10]

The solid electrolyte interphase has extensively been studied in the context of lithium- and sodium-ion batteries, where it forms spontaneously from electrolyte decomposition at the electrode surface[11–15] (Scheme 1). Classical reports described the SEI as a heterogeneous, nanometer-scale layer composed of both inorganic and organic species, including Si–N-MXene, Si@SiO_2@LPO@C, LiF, Li_3N, and Li_2O.[11–15] Its stability is critical for suppressing continuous electrolyte reduction,

---

[a] *Departamento de Física, Facultad de Ciencias Naturales y Exactas, Universidad de Oriente, CP 90500, Santiago de Cuba, Cuba*
[b] *Laboratory for Chemical Computation and Modeling, Institute for Computational Science and Artificial Intelligence, Van Lang University, Ho Chi Minh City, 70000, Vietnam. E-mail: minhtho.nguyen@vlu.edu.vn*
[c] *Faculty of Applied Technology, Van Lang School of Technology, Van Lang University, Ho Chi Minh City, 70000, Vietnam*

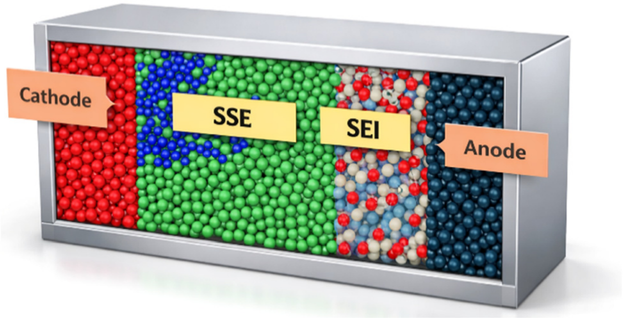

Scheme 1 Main components of a metal ion battery.

maintaining low interfacial impedance, and enabling long cycle life.[11–15] Over the past two decades, research has focused on tailoring SEI composition through electrolyte additives, solvent engineering, and artificial interphases to improve mechanical integrity and ionic transport.[11–15]

The SEI is central to the long-term stability of rechargeable batteries, yet its effectiveness depends on meeting several stringent requirements. An ideal SEI must be mechanically robust to withstand electrode volume changes, while sufficiently ductile and isotropic to prevent cracking and interfacial delamination.[11–15] It should combine low elastic anisotropy and favorable machinability to minimize stress accumulation in polycrystalline domains, while maintaining high chemical stability against both electrodes and electrolytes. In addition, the SEI must allow facile alkali-ion transport but remain electronically insulating to suppress further electrolyte decomposition.[11–18] Meeting these diverse criteria simultaneously remains a major challenge, motivating the exploration of new halide-based phases as potential SEI constituents.[4,11,12] Inorganic-rich SEIs are generally more robust, while organic-rich SEIs provide flexibility but weaker passivation.[4,11,12] However, complex halide phases beyond simple fluorides have not been explicitly reported as SEI components, leaving a gap in the exploration of ternary halides as interfacial stabilizers.

Beyond simple halides, a growing family of complex halide compounds has been investigated as SSE and interfacial stabilizers in rechargeable batteries.[19–22] Chloride-based conductors such as Li_3InCl_6, Li_3YCl_6 and Li_3ErCl_6 demonstrated their high ionic conductivity and excellent chemical stability, making them attractive candidates for all-solid-state lithium batteries.[19–22] Similarly, sodium-rich halides like Na_2ZrCl_6 have been shown to enhance interfacial compatibility and transport properties in sodium ion systems.[23,24] Mixed halide frameworks that incorporate both chloride and bromide ions are also being explored to tune up the lattice flexibility and optimize Na^+ or Li^+ mobility.[19–24] Perhaps more importantly, the surface orientation of these halide compounds plays a decisive role in their interfacial behaviour, as different crystallographic facets exhibit distinct defect formation energies, ionic transport pathways, and mechanical responses. By carefully controlling surface termination and orientation, we can tailor interfacial stability and conductivity, ensuring that halide-based solid electrolytes deliver both robust passivation and efficient ion migration.[25–28] These advances highlight that halide chemistry extends well beyond simple binary salts, with ternary and quaternary halides offering unique opportunities to balance mechanical robustness, ionic conductivity, and interfacial stability.[25–30]

Atomistic simulations are increasingly important for predicting the fundamental properties of battery materials, as they provide us with a direct link between crystal structure and functional behaviour without requiring experimental validation.[31–42] Static force-field computations, in particular, allow the quantification of defect energetics such as vacancy formation and dopant substitution energies, clarifying the thermodynamic feasibility of structural modifications and their impact on stability.[31,33,35] Complementing this, the bond valence site energy (BVSE) analyses map bond valence site energies to identify favourable migration pathways and activation barriers, thereby revealing anisotropy in ionic conduction and showing how defect structures reshape transport channels.[39–42] By combining defect energetics with transport landscapes, atomistic simulations establish a concise framework for evaluating both stability and ionic conductivity, offering a powerful tool for guiding the design of SSEs and electrode architectures in next-generation energy storage systems.[39–42] These combined approaches have been used to disclose properties of various halide containing compounds.[33,35,43,44]

Previous studies on $NaMgCl_3$ and $NaMgBr_3$ have primarily focused on their optoelectronic and thermodynamic performances in the cubic Pm-3m phase, motivated by potential applications in photovoltaics and related fields.[45–47] In contrast, their role as SEI candidates in sodium ion batteries has not been investigated in the trigonal $R\bar{3}$ phase, leaving an unexplored opportunity for assessing their stability and defect chemistry under electrochemical conditions. In addition, the possibility of modelling the hypothetical $NaMgBr_3$ phase through atomistic simulations provides a complementary perspective, enabling predictive assessment of defect energetics and transport pathways in a system not yet experimentally confirmed. As in our previous work,[44] the Br^- anion force-field has been proven to be reliable for reproducing structural and energetic trends in related halides, which supports the feasibility of extending this computational framework to $NaMgBr_3$ and evaluating its potential as an SEI candidate alongside $NaMgCl_3$.

The aim of this work is to evaluate the defect energetics, mechanical and surface stability, and transport properties of halide compounds relevant to sodium ion batteries, with emphasis on $NaMgCl_3$ and the hypothetical $NaMgBr_3$ phase. While $NaMgCl_3$ has been reported in the literature as a structurally stable material, its potential role as an SEI has not yet been investigated. Building on our previous validation of Br^- force-field parameters, we extend atomistic simulations to $NaMgBr_3$ to predict its defect chemistry, mechanical resilience, surface energetics, and conduction pathways. By combining static force-field calculations with BVSE analyses, this study emphasizes the energetic feasibility of defect formation, the anisotropy of ionic transport, and the correlation between mechanical and surface stability with conducting properties, thereby providing a novel framework for assessing halide compounds as an SEI in next-generation sodium-ion cells.

2. Materials and methods

To investigate the structural, electronic and mechanical properties of $NaMgX_3$ structures, density functional theory (DFT) calculations are conducted using the CASTEP code.[48] The PBE Optimized for Solids (PBESOL) exchange–correlation functional within the generalized gradient approximation (GGA) is employed.[49] On-the-fly generation (OTFG) ultrasoft pseudopotentials with a plane-wave energy cutoff of 517 eV are utilized. The pseudoatomic functions for Na-$2s^22p^63s^1$, Mg-$2p^63s^2$, and X-$3s^23p^5$ in reciprocal space represent electronic configurations of the constituent atoms. The convergence criteria are set to ensure reliable optimization, with thresholds of less than 5×10^{-6} eV per atom for total energy change, maximum residual forces below 10^{-2} eV Å^{-1}, stresses under 2×10^{-2} GPa, and atomic displacements limited to 5×10^{-4} Å. A $4 \times 4 \times 4$ Monkhorst–Pack *k*-point mesh is employed to sample the Brillouin zone,[50] providing sufficient reciprocal-space resolution for accurate total energy and electronic structure calculations.

In addition, the General Utility Lattice Program (GULP) is used to explore lattice parameters, mechanical properties as well as the formation of intrinsic defects.[51] The force-field is adopted from previous reports.[44,52,53] Buckingham potential is used for modelling the short-range interactions. Coulombic forces are considered for long-range interactions, where the charge and the interatomic distance between species describe the long-range potential energy. The shell model is used for dealing with the ionic polarization.[54] The shell model considers each ion as a positively core and a negatively shell charged coupled by a spring (with spring constant *k*), where the sum of the core–shell charge results in the formal charge (Z) of the ion.[54] The force-field parameters are given in the supplementary information (SI) file.

The Mott-Littleton method is employed for defect calculations.[55] In this approach, the crystal lattice is partitioned into two concentric spherical regions with radii R_1 and R_2 ($R_1 < R_2$). The isolated defect or defect cluster is located within the inner sphere R_1 where strong local interactions between the defect and neighbouring atoms are explicitly considered. The outer region R_2 is treated using a quasi-continuum approximation.[51,56] The radii are set to R_1 = 14 Å and R_2 = 27 Å to ensure computational accuracy because the radius R_1 and the difference R_2–R_1 must exceed the maximum short-range cutoff of the interatomic potential. The geometry optimization and defect energetics are carried out using the Broyden–Fletcher–Goldfarb–Shanno (BFGS) algorithm, updating the lattice parameters and atomic positions iteratively. In this formalism, the defect is treated at the infinitely dilute limit avoiding interactions between defects.[51,56]

The total defect formation energy E_T is expressed as in eqn (1):[51,56]

$$E_T = E_1(x) + E_{12}(x,\varepsilon) + E_2(\varepsilon) \tag{1}$$

where x and ε represent interatomic displacements in the inner and outer regions, E_1 and E_2 are the energy contributions from regions R_1 and R_2, respectively, while E_{12} represents the interchange energy between the regions.

The defect chemistry, specifically the formation energy of basic defects such as Schottky- and Frenkel-type defects, is related to the electrochemical behaviour of battery materials.[1–10] In this context, we consider various schemes describing their formation energies. Three Schottky defect mechanisms are considered. The first involves the full $NaMgX_3$ Schottky scheme, written in the Kröger–Vink notation,[57] as described by eqn (2):

$$\mathrm{Na}_{\mathrm{Na}}^{\times} + \mathrm{Mg}_{\mathrm{Mg}}^{\times} + 3\mathrm{X}_{\mathrm{X}}^{\times} \rightarrow \mathrm{V}_{\mathrm{Na}}' + \mathrm{V}_{\mathrm{Mg}}'' + 3\mathrm{V}_{\mathrm{X}}^{\bullet} + \mathrm{NaMgX}_3 \tag{2a}$$

$$E_s = \frac{1}{3}\left(E_{\mathrm{vac}}^{\mathrm{Na}} + E_{\mathrm{vac}}^{\mathrm{Mg}} + 3E_{\mathrm{vac}}^{\mathrm{X}} + E_{\mathrm{L}}^{\mathrm{NaMgX_3}}\right) \tag{2b}$$

From now on, expressions below a semi chemical equation (such as (2a)) represent the solution energy. In eqn (2a) $\mathrm{Mg}_{\mathrm{Mg}}^{\times}$, $\mathrm{Na}_{\mathrm{Na}}^{\times}$ and $\mathrm{X}_{\mathrm{X}}^{\times}$ represent the constituent ions occupying their respective atomic positions at the $NaMgCl_3$ lattice structure, while $\mathrm{V}_{\mathrm{Na}}'$, $\mathrm{V}_{\mathrm{Mg}}''$ and $\mathrm{V}_{\mathrm{X}}^{\bullet}$ symbolize Na^+, Mg^{2+} and Cl^- (or Br^-) vacancies, while in eqn (2b), $E_{\mathrm{vac}}^{\mathrm{Na}}$, $E_{\mathrm{vac}}^{\mathrm{Mg}}$, and $E_{\mathrm{vac}}^{\mathrm{X}}$ their formation energy and $E_{\mathrm{L}}^{\mathrm{NaMgX_3}}$ the lattice energy of $NaMgX_3$, respectively.

Formation of a NaX Schottky defect is described by eqn (3):

$$\mathrm{Na}_{\mathrm{Na}}^{\times} + \mathrm{X}_{\mathrm{X}}^{\times} \rightarrow \mathrm{V}_{\mathrm{Na}}' + \mathrm{V}_{\mathrm{X}}^{\bullet} + \mathrm{NaX} \tag{3a}$$

$$E_s = \frac{1}{2}\left(E_{\mathrm{vac}}^{\mathrm{Na}} + E_{\mathrm{vac}}^{\mathrm{X}} + E_{\mathrm{L}}^{\mathrm{NaX}}\right) \tag{3b}$$

where $E_{\mathrm{L}}^{\mathrm{NaX}}$ represent the lattice energy of the NaX compound.

The third basic scheme describes the formation of the MgX_2 Schottky defect as in eqn (4):

$$\mathrm{Mg}_{\mathrm{Mg}}^{\times} + 2\mathrm{X}_{\mathrm{X}}^{\times} \rightarrow \mathrm{V}_{\mathrm{Mg}}'' + 2\mathrm{V}_{\mathrm{X}}^{\bullet} + \mathrm{MgX}_2 \tag{4a}$$

$$E_s = \frac{1}{2}\left(E_{\mathrm{vac}}^{\mathrm{Mg}} + 2E_{\mathrm{vac}}^{\mathrm{X}} + E_{\mathrm{L}}^{\mathrm{MgX_2}}\right) \tag{4b}$$

where $E_{\mathrm{L}}^{\mathrm{MgX_2}}$ symbolizes the lattice energy of MgX_2.

In addition, the Na^+ Frenkel type mechanism explains the excess of Na^+, increasing the Na concentration as described by eqn (5):

$$\mathrm{Na}_{\mathrm{Na}}^{\times} \rightarrow \mathrm{V}_{\mathrm{Na}}' + \mathrm{Na}_{\mathrm{i}}^{\bullet} \tag{5a}$$

$$E_s = \frac{1}{2}\left(E_{\mathrm{vac}}^{\mathrm{Na}} + E_{\mathrm{inter}}^{\mathrm{Na}}\right) \tag{5b}$$

and with Li interstitials:

$$\mathrm{Na}_{\mathrm{Na}}^{\times} \rightarrow \mathrm{V}_{\mathrm{Na}}' + \mathrm{Li}_{\mathrm{i}}^{\bullet} \tag{5c}$$

$$E_{\mathrm{s}} = \frac{1}{2}\left(E_{\mathrm{vac}}^{\mathrm{Na}} + E_{\mathrm{inter}}^{\mathrm{Li}}\right) \tag{5d}$$

where for each Na^+ vacancy, an extra Na^+ or Li^+-ion occupying an interstitial site $\left(\mathrm{Na}_{\mathrm{i}}^{\bullet}, \mathrm{Li}_{\mathrm{i}}^{\bullet}\right)$ with energy $\left(E_{\mathrm{inter}}^{\mathrm{Na}}, E_{\mathrm{inter}}^{\mathrm{Li}}\right)$ is required for charge compensation.

Another interesting scheme is to consider the Li^+ substitution at Na^+-site $\left(\mathrm{Li}_{\mathrm{Na}}^{\times}\right)$ with energy $E_{\mathrm{Na}}^{\mathrm{Li}}$ in $\mathrm{NaMgX_3}$, as in eqn (6):

$$\mathrm{LiX} + \mathrm{Na}_{\mathrm{Na}}^{\times} \rightarrow \mathrm{Li}_{\mathrm{Na}}^{\times} + \mathrm{NaX} \tag{6a}$$

$$E_{\mathrm{s}} = E_{\mathrm{Na}}^{\mathrm{Li}} + E_{\mathrm{L}}^{\mathrm{NaX}} - E_{\mathrm{L}}^{\mathrm{LiX}} \tag{6b}$$

where $E_{\mathrm{L}}^{\mathrm{NaX}}$ and $E_{\mathrm{L}}^{\mathrm{LiX}}$ are the lattice energies of LiX and NaX, respectively.

The substitution of a Li^+-ion at a Mg^{2+}-site in the $\mathrm{NaMgX_3}$ lattice structure leading to an X-vacancy is given by eqn (7):

$$\mathrm{LiCl} + \mathrm{Mg}_{\mathrm{Mg}}^{\times} + \mathrm{X}_{\mathrm{X}}^{\times} \rightarrow \mathrm{Li}_{\mathrm{Mg}}^{\bullet} + \mathrm{V}_{\mathrm{X}}^{\bullet} + \mathrm{MgX_2} \tag{7a}$$

$$E_{\mathrm{s}} = \frac{1}{2}\left(E_{\mathrm{Mg}}^{\mathrm{Li}} + E_{\mathrm{vac}}^{\mathrm{X}} + E_{\mathrm{L}}^{\mathrm{MgX_2}} - E_{\mathrm{L}}^{\mathrm{LiX}}\right) \tag{7b}$$

Analogously, substitution of a Na^+-ion at the Mg^{2+}-site in the $\mathrm{NaMgX_3}$ lattice structure leading to an X-vacancy is given by eqn (8):

$$\mathrm{NaX} + \mathrm{Mg}_{\mathrm{Mg}}^{\times} + \mathrm{X}_{\mathrm{X}}^{\times} \rightarrow \mathrm{Na}_{\mathrm{Mg}}^{\bullet} + \mathrm{V}_{\mathrm{X}}^{\bullet} + \mathrm{MgX_2} \tag{8a}$$

$$E_{\mathrm{s}} = \frac{1}{2}\left(E_{\mathrm{Mg}}^{\mathrm{Na}} + E_{\mathrm{vac}}^{\mathrm{X}} + E_{\mathrm{L}}^{\mathrm{MgX_2}} - E_{\mathrm{L}}^{\mathrm{NaX}}\right) \tag{8b}$$

With the potential parameters availability for divalent and trivalent cations,[43,44] we explore potential defect chemistry formation of divalent (M^{2+} = Zn^{2+}, Ca^{2+}, Sr^{2+}) and trivalent (A^{3+} = Al^{3+}, Ga^{3+}) in different compensation schemes. A divalent doping (M^{2+}) occupying a Mg^{2+}-site in the $\mathrm{NaMgX_3}$ lattice structure is given by eqn (9):

$$\mathrm{MX_2} + \mathrm{Mg}_{\mathrm{Mg}}^{\times} \rightarrow \mathrm{M}_{\mathrm{Mg}}^{\times} + \mathrm{MgX_2} \tag{9a}$$

$$E_{\mathrm{s}} = E_{\mathrm{subs,Mg}}^{\mathrm{M}^{2+}} + E_{\mathrm{L}}^{\mathrm{MgX_2}} - E_{\mathrm{L}}^{\mathrm{MX_2}} \tag{9b}$$

The scheme of inclusion of an M^{2+} dopant at a Na^+-site in $\mathrm{NaMgX_3}$ lattice structure is given by eqn (10):

$$\mathrm{MX_2} + 2\mathrm{Na}_{\mathrm{Na}}^{\times} \rightarrow \mathrm{M}_{\mathrm{Na}}^{\bullet} + \mathrm{V}_{\mathrm{Na}}^{\prime} + 2\mathrm{NaX} \tag{10a}$$

$$E_{\mathrm{s}} = E_{\mathrm{subs,Na}}^{\mathrm{M}^{2+}} + E_{\mathrm{vac}}^{\mathrm{Na}} + 2E_{\mathrm{L}}^{\mathrm{NaX}} - E_{\mathrm{L}}^{\mathrm{MX_2}} \tag{10b}$$

in which for each divalent dopant occupying a Na^+-site $\left(\mathrm{M}_{\mathrm{Na}}^{\bullet}\right)$, a Na^+ vacancy is created for charge balancing, favoring the formation of $\mathrm{M}_{\mathrm{Na}}^{\bullet} - \mathrm{V}_{\mathrm{Na}}^{\prime}$ pair defect.

The introduction of a trivalent dopant (A^{3+}) at a Na^+-site $\left(\mathrm{A}_{\mathrm{Na}}^{\bullet\bullet}\right)$ is given by eqn (11):

$$\mathrm{AX_3} + 3\mathrm{Na}_{\mathrm{Na}}^{\times} \rightarrow \mathrm{A}_{\mathrm{Na}}^{\bullet\bullet} + 2\mathrm{V}_{\mathrm{Na}}^{\prime} + 3\mathrm{NaX} \tag{11a}$$

$$E_{\mathrm{s}} = \frac{1}{3}\left(E_{\mathrm{subs,Na}}^{\mathrm{A}^{3+}} + 2E_{\mathrm{vac}}^{\mathrm{Na}} + 3E_{\mathrm{L}}^{\mathrm{NaX}} - E_{\mathrm{L}}^{\mathrm{AX_3}}\right) \tag{11b}$$

in which for each A^{3+}, substituting a Na^+-site requires two Na^+-vacancies for charge compensation.

The next incorporation mechanism deals with the introduction of a trivalent dopant occupying an Mg^{2+}-site as in eqn (12):

$$\mathrm{AX_3} + \mathrm{Mg}_{\mathrm{Mg}}^{\times} + \mathrm{Na}_{\mathrm{Na}}^{\times} \rightarrow \mathrm{A}_{\mathrm{Mg}}^{\bullet} + \mathrm{V}_{\mathrm{Na}}^{\prime} + \mathrm{MgX_2} + \mathrm{NaX} \tag{12a}$$

$$E_{\mathrm{s}} = \frac{1}{3}\left(E_{\mathrm{subs,Mg}}^{\mathrm{A}^{3+}} + E_{\mathrm{vac}}^{\mathrm{Na}} + E_{\mathrm{L}}^{\mathrm{NaX}} + E_{\mathrm{L}}^{\mathrm{MgX_2}} - E_{\mathrm{L}}^{\mathrm{AX_3}}\right) \tag{12b}$$

where for each trivalent dopant replacing a Mg^{2+} -site, one Na^+-vacancy is needed for charge compensation.

Furthermore, the bond valence method offers an intuitive and robust approach for identifying diffusion pathways and estimating activation energies associated with ionic conduction mechanisms.[39–42,58] This methodology pinpoints mobile sodium ions by locating regions of minimal bond valence site energy. The bond length between sodium (Na^+) and halide (X^-), denoted as $L_{\mathrm{Na-X}}$, is assessed using the reference bond length ($L_{0,\mathrm{Na-X}}$) and bond softness parameter ($b_{\mathrm{Na-X}}$),[39–42,58] which correlate with the individual bond valence contribution ($s_{\mathrm{Na-X}}$) *via* eqn (13):

$$s_{\mathrm{Na-X}} = \exp\left[\left(L_{0,\mathrm{Na-X}} - L_{\mathrm{Na-X}}\right)/b_{\mathrm{Na-X}}\right] \tag{13}$$

The bond-valence site energy of sodium ions, $E_{\mathrm{BV}}(\mathrm{Na})$, is then calculated in analogy to Morse-type potentials,[39–42,58] augmented by the Coulombic repulsion term E_{r} arising from interactions between mobile Na^+ and surrounding immobile framework cation Mg^{2+}. This is expressed in eqn (14):

$$E_{\mathrm{BV}}(\mathrm{Na}) = \sum_{\mathrm{X}} D_0 \left[\sum_{i=1}^{N}\left[\left(s_{\mathrm{Na-X}}/s_{\mathrm{min,Na-X}}\right)^2 - 2s_{\mathrm{Na-X}}\Big/s_{\mathrm{min,Na-X}}\right]\right] + E_{\mathrm{r}} \tag{14}$$

where D_0 is the bond dissociation energy constant and $s_{\mathrm{min,Na-X}}$ is the optimal bond valence corresponding to the shortest energetically favourable Na^+–X^- separation.[39–42,55] The summation over X^- accounts for all coordinating halide ions within the local environment of the migrating Na^+. The Coulombic term E_{r} introduces a penalty for proximity to other mobile Na^+-ions, effectively modelling repulsion and preventing artificial clustering in the energy landscape. This energy expression defines the potential surface over which Na^+ migration is evaluated. Local minima correspond to energetically favourable sites, while saddle points represent transition states. The resulting BVSE map enables rapid identification of conduction pathways and estimation of migration barriers.[39–42,58]

The softBV-GUI tool is used to analyse the sodium mobility within the structures considered.[58] The required parameters from eqn (13) and (14) are integrated into the softBV-GUI code. In these systems, Coulombic repulsions between mobile Na^+ ions and immobile divalent cations (Mg^{2+}) are duly considered. Attractive interactions, such as Na^+–X^- Coulombic terms, are inherently embedded within the Morse-type potential framework. Migration paths for Na^+ ions follow regions of low bond valence site energy in mesh grids wrapping the $\mathrm{NaMgX_3}$ lattice structures with a resolution of ± 0.1 Å^3. For a comprehensive treatment of the bond valence methodology and its application in halide frameworks, readers are referred to the foundational and recent literature.[39–42,58] The procedures adopted in this work have been proven effective for modelling defect formation energies and prompt estimation of transport properties in solid-state battery materials.[39–44]

Under the BVSE approach, the diffusion coefficient is computed based on the dimensionality of the migration path as follows (eqn (15)):[58]

$$D = \sum_{d=1}^{3} \frac{\alpha^2}{2d}\nu_d \left[\exp\left(\frac{E_{\mathrm{mig},d} + E_{\mathrm{def},d}}{RT}\right) + 1\right]^{-1} \quad (15)$$

where α is the hop distance equal to the sum of the covalent radius of mobile cation and anion, $E_{\mathrm{def},d}$ symbolizes the defect formation energy according to the pathway of dimensionality d (*i.e.*; 1, 2 and 3 for 1-, 2- and 3D migration pathways, respectively), ν_d is the attempt frequency, R is the gas constant and $E_{\mathrm{mig},d}$ is the migration energy of the mobile ion for the pathway of d-dimension and T is the absolute temperature.[39–42,58] The global diffusion coefficient is the sum of the diffusivity computed by eqn (15) in each dimensionality. The conductivity is then computed by using the Nernst–Einstein relation as implemented in the softBV-GUI code.[58] As expected, both diffusion and conduction follow an Arrhenius-type dependence with respect to temperature.[58]

Surface calculations are performed using the GULP code as well to determine the most stable surface of $NaMgX_3$. Slab models are generated by cleaving the optimized bulk structures along low-index crystallographic planes, including (100), (010), (001), (110), (111), and (210). Other crystallographic planes are equivalent in the compound with the $R\bar{3}$ space group. According to the lattice structure and composition, a vacuum spacing was introduced perpendicular to the surface normal to avoid spurious interactions between periodic images. All slabs are fully relaxed under constant-pressure conditions using the BFGS algorithm, ensuring convergence of both atomic positions and lattice vectors.

The surface energy (γ) was computed according to:

$$\gamma = (E_{\mathrm{slab}} - NE_{\mathrm{bulk}})/2A \quad (16)$$

where E_{slab} is the total energy of the relaxed slab, E_{bulk} is the energy per formula unit of the bulk structure, N is the number of formula units contained in the slab, and A is the surface area. The factor of 2 accounts for the two equivalent surfaces present in the slab model. Convergence tests are performed with respect to slab thickness and vacuum spacing to ensure numerical stability of γ values.

Following identification of the most stable surface, the bond valence site energy method was applied in order to evaluate Na$^+$ transport properties under realistic interfacial conditions. This combined approach ensures that transport analysis reflects not only bulk energetics but also the anisotropy and structural constraints imposed by the dominant surface termination.

3. Results and discussion

3.1. Structural and electronic properties of pristine $NaMgX_3$ structures

Fig. 1a displays the unit cell of $NaMgX_3$ structures in the hexagonal representation. $NaMgCl_3$ is ilmenite-type and belongs to the $R\bar{3}$ space group (space group number 148), with six formula units per unit cell ($Z = 6$).[59] These compounds adopt a three-dimensional environment where Mg^{2+} and Na$^+$ ions are six coordinated by chloride ions. We used $NaMgCl_3$ as a parent structure to study the existence of $NaMgBr_3$ with the same framework.

Table 1 collects the optimized lattice parameters for $NaMgX_3$ obtained with the FF model and DFT computations, referenced to the experimental $NaMgCl_3$ structure.[59] For $NaMgCl_3$ the FF optimization returns $a = b = 6.289$ Å and $c = 18.339$ Å (FF deviations *vs.* experiment: a = b = 3.34%, c = 1.33%), whereas DFT gives $a = b = 6.425$ Å and $c = 19.401$ Å (DFT deviations vs experiment: a = 1.24%, c = 4.39%). On substitution of Cl by Br predict a pronounced, anisotropic expansion: FF yields $NaMgBr_3$ $a = b = 7.423$ Å and $c = 20.537$ Å (expansions of 14.09 and 10.50% relative to the $NaMgCl_3$ reference), while DFT gives $a = b = 6.855$ Å and $c = 20.935$ Å (expansions of 5.36% and 12.64%). The two approaches therefore agree qualitatively with each other on the anisotropic dilation of the $R\bar{3}$ cell on halide substitution, with FF systematically predicting a larger in-plane expansion, and DFT providing a more moderate quantitative estimate for the a-parameter but a comparable elongation of the c-axis. The comparative analysis demonstrates that the FF method captures the essential structural trends across halide variants, with FF offering computational efficiency.

Table 1 reports the [MgX_6] octahedral geometry obtained from both FF and DFT optimizations; the two methods yield the same structural picture and the numerical differences between them are small and not significant for the conclusions drawn. For $NaMgCl_3$, FF gives an average bond length (L) of 2.42 Å and

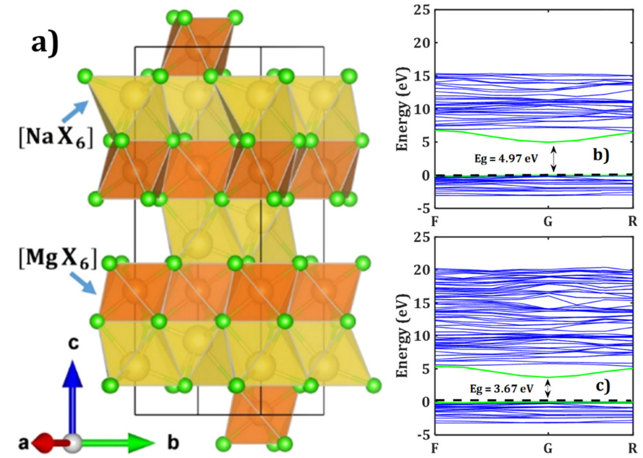

Fig. 1 (a) Hexagonal representation of $NaMgX_3$ (space group $R\bar{3}$) and band structure of (b) $NaMgCl_3$ and (c) $NaMgBr_3$ compounds, respectively. The dashed black line represents the Fermi level.

Table 1 Lattice parameters (in Å) of optimized $NaMgX_3$ (space group $R\bar{3}$) structures derived from geometry optimization derived from FF and DFT (in brackets) computations. The Δ-values represent the deviations of lattice parameters with respect to those reported for $NaMgCl_3$ in ref. 59

Structure	A	b	c
$NaMgCl_3$	6.289 (6.425)	6.289 (6.425)	18.339 (19.401)
Δ (%)	+3.341 (+1.241)	+3.341 (+1.241)	+1.328 (+4.388)
$NaMgBr_3$	7.423 (6.855)	7.423 (6.855)	20.537 (20.935)
Δ (%)	14.088 (+5.363)	14.088 (+5.363)	10.496 (+12.640)
ref. 59	6.506	6.506	18.586

Structure	V (Å^3)	L (Å)	Ω ($^{\circ 2}$)	d_i	Q	ECN
$NaMgCl_3$	18.253 (21.438)	2.420 (2.522)	78.031 (15.380)	0.005 (0.009)	1.023 (1.004)	5.995 (5.983)
$NaMgBr_3$	32.88 (26.303)	2.922 (2.706)	27.798 (11.303)	0.016 (0.005)	1.008 (1.003)	5.947 (5.995)

Octahedral volume (V), average bond length (L), bond angle variance (Ω), distortion index (d_i) quadratic elongation (Q) and effective coordination number (ECN) of $[MgCl_6]$ octahedral in $NaMgX_3$ ($M = Cl^-$, Br^-) structures derived from FF and DFT (in brackets) computations.

an octahedral volume (V) of 18.25 Å^3, while DFT returns 2.52 Å and V = 21.44 Å^3. The absolute offset of 4.2% is modest and does not change the assignment of a compact, near-sixfold Mg coordination in the chloride.

The angular and distortion descriptors are likewise consistent, namely, FF reports a bond-angle variance (Ω) of $78.0^{\circ 2}$, distortion index (d_i) of 0.005, quadratic elongation (Q) of 1.023, and effective coordination number (ECN) of 5.995, while DFT yields $\Omega = 15.4^{\circ 2}$, $d_i = 0.009$, $Q = 1.004$, and ECN = 5.983. These values confirm a nearly ideal octahedral environment with only minor quantitative differences between methods.

For $NaMgBr_3$, both methods again agree with each other on an expanded Mg coordination environment. FF reports L = 2.922 Å and V = 32.88 Å^3, whereas DFT gives L = 2.706 Å and V = 26.30 Å^3. Although the DFT-FF deviations for the bromide are larger in magnitude, they remain quantitative refinements rather than in contradiction with the physical trend that Br^- produces substantially larger octahedra than Cl^-. The angular and distortion metrics support this interpretation: FF yields $\Omega = 27.8^{\circ 2}$, $d_i = 0.016$, $Q = 1.008$, and ECN = 5.947, while DFT gives $\Omega = 11.3^{\circ 2}$, $d_i = 0.005$, $Q = 1.003$, and ECN = 5.995.

Both descriptions indicate that Br substitution reduces angular variance and maintains near-ideal elongation and coordination, highlighting a more regular but expanded octahedral geometry.

To make the comparison transparent in the manuscript, the numerical spread between FF and DFT should be presented as a bracket on each reported metric. In practice this means quoting the FF and DFT values side by side and, where useful, giving the range spanned by the two methods as an uncertainty interval. Treating the paired FF and DFT results as lower and upper bounds provides a conservative estimate of structural uncertainty arising from methodological choice and gives readers a clear sense of the numerical spread without implying a single true value.

The geometric descriptors of the $[MgX_6]$ octahedra in $NaMgX_3$ structures reveal pronounced structural differences that stem primarily from the ionic size and polarizability of the halide anions. The larger ionic radius of Br^- compared to Cl^- leads to an expanded octahedral volume and longer average Mg–Br bond lengths, consistent with the expected lattice dilation upon halide substitution.

This expansion reduces angular distortion, as evidenced by the lower bond angle variance in $NaMgBr_3$ relative to $NaMgCl_3$, suggesting a more regular angular distribution despite the increased bond length. However, the distortion index and effective coordination number indicate that $NaMgBr_3$ exhibits slightly greater deviation from ideal octahedral symmetry and marginally reduced coordination, likely due to enhanced anion polarizability and weaker electrostatic interactions in the Br^--rich environment.

These factors collectively contribute to a softer, more deformable lattice in $NaMgBr_3$, which may influence defect formation energies and facilitate ionic migration. The interplay between ionic size, bond strength, and lattice flexibility thus underpins the structural divergence observed across the $NaMgX_3$ series and informs their respective transport and mechanical behaviours.

The metrics to explore electronic properties are the analysis of band structure and density of states. Fig. 1b and c show the band structures of $NaMgX_3$ compounds. Exploration of electronic properties is of vital importance to decide the applicability of a compound as an SEI.[1–10] In this context, the SEI should suppress electronic conduction while allowing selective ionic transport, ensuring electrochemical stability at the electrode contact.[1–10]

For $NaMgCl_3$ (Fig. 1b), the valence bands extend up to the Fermi level, with conduction bands beginning near 4.97 eV. The calculated band gap of E_g = 4.97 eV indicates negligible electronic conductivity, consistent with the role of a passivating SEI. In $NaMgBr_3$ (Fig. 1c), the band gap narrows to E_g = 3.67 eV, reflecting weaker Mg–Br bonding and higher polarizability of Br^-. Although smaller than the chloride, this gap still lies within the insulating regime, confirming that both halides suppress electronic conduction at the interface.

These values align with the general criteria for considering halide compounds as SEI phases: wide band gaps, minimal electronic transport, and stability under operating conditions. In view of the usual underestimation of DFT calculations and the lack of experimental results, the reported E_g values should

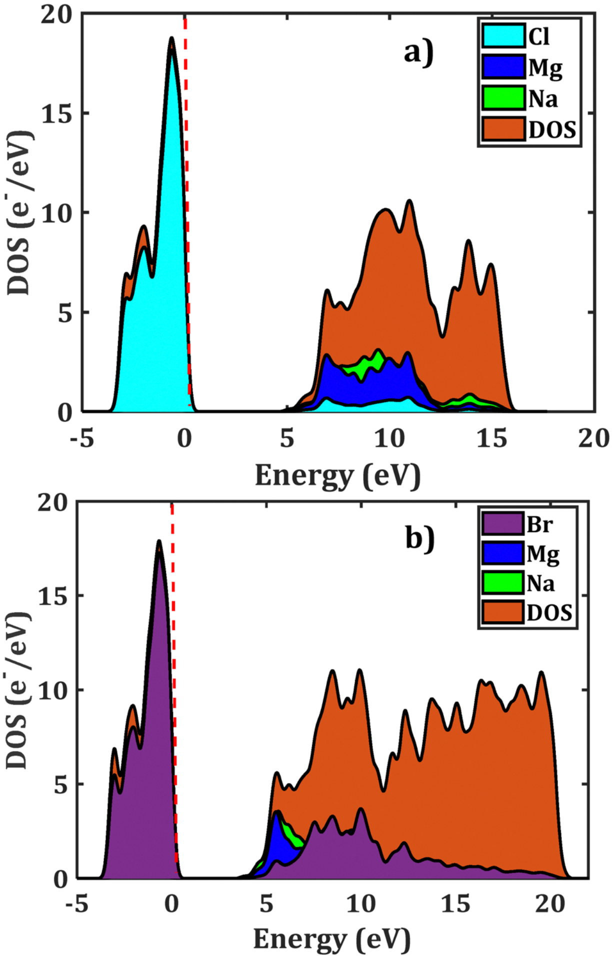

Fig. 2 Density of states (DOS) of (a) $NaMgCl_3$ and (b) $NaMgBr_3$ structures. The dashed red line represents the Fermi level.

be considered lower bounds. The comparison between $NaMgCl_3$ and $NaMgBr_3$ highlights the trade-off between band gap magnitude and structural expansion, reinforcing the conclusion that both compounds act as electronically insulating interphases suitable for sodium SEI.

Fig. 2 shows the density of states (DOS) for $NaMgX_3$ structures, highlighting the orbital contributions of halide, Mg, and Na atoms. In $NaMgCl_3$ (Fig. 2a), the valence band region (−5 to 0 eV) is dominated by Cl-p states, with minor contributions from Mg-s and Na-s orbitals. The conduction band onset near 4.9 eV is primarily composed of Mg-p and Na-p states, consistent with the wide band gap observed in the band structure. This separation between halide-dominated valence states and cation-dominated conduction states reinforces the insulating character of the chloride phase.

For $NaMgBr_3$ (Fig. 2b), the valence band is shifted upward due to the higher polarizability and lower electronegativity of Br, resulting in a narrower band gap of 3.67 eV. The valence region shows strong Br-p contributions, while the conduction band edge again involves Mg-p and Na-p states. The reduced gap compared to $NaMgCl_3$ reflects weaker Mg–Br bonding and enhanced orbital overlap, but the DOS profile still indicates a negligible electronic conduction.

The DOS analysis confirms that both halides exhibit localized halogen-p valence states and cation-dominated conduction states, with minimal hybridization across the gap. Such an electronic structure is consistent with their role as electronically insulating phases at the SEI, where suppression of electronic transport is essential to maintain ionic selectivity and interfacial stability.

3.2. Intrinsic defect formation and doping strategies of $NaMgX_3$ structures

Table 2 summarizes the calculated solution energies for a range of intrinsic and aliovalent defect mechanisms in $NaMgX_3$ lattice structures, revealing clear thermodynamic trends that govern its defect chemistry. The comparative defect energetics of $NaMgCl_3$ and $NaMgBr_3$ reveal distinct thermodynamic behaviour shaped by the halide identity and lattice flexibility. In $NaMgCl_3$, Na^+ and Cl^- vacancies are the most favourable intrinsic defects, with formation energies of 4.54 eV and 4.98 eV per defect, respectively, while Mg^{2+} vacancies are highly unfavourable at 21.81 eV per defect. This indicates that the Mg sublattice is rigid and resistant to defect formation. In $NaMgBr_3$, the expanded $[MgBr_6]$ octahedron and softer lattice reduce defect formation energies, making Na^+ and Br^- vacancies more accessible and suggesting a higher concentration of mobile carriers under similar conditions.

The full Schottky scheme in $NaMgCl_3$ is strongly negative (−9.27 eV per defect), highlighting its instability toward decomposition. Specifically, $NaMgCl_3$ decomposes into Na_6MgCl_8 and $MgCl_2$, consistent with computational predictions.[60] In $NaMgBr_3$, analogous decomposition pathways are expected, with the compound destabilizing into Na_6MgBr_8 and $MgBr_2$. The larger ionic radius and polarizability of Br^- reduce energetic penalties, making defect formation and decomposition more favorable compared to the chloride analogue. Isolated Schottky schemes for NaX and MgX_2 remain favourable in both compounds, but the bromide variant shows reduced energetic barriers, reinforcing its softer lattice character.

Frenkel-type mechanisms are accessible in both halides. In $NaMgCl_3$, the Na^+ Frenkel pair exhibits a moderate formation energy of 0.69 eV per defect, while the Li^+ interstitial variant is even more favourable at 0.34 eV per defect. Substitutional Li^+ at the Na^+-site is particularly favoured (0.10 eV per defect). In $NaMgBr_3$, the expanded lattice further lowers Frenkel and interstitial defect energies, facilitating Na^+ migration. The softer Br^- environment stabilizes interstitial carriers, suggesting improved ionic conductivity compared to $NaMgCl_3$.

Divalent doping strategies show consistent trends across both halides but are energetically more convenient in $NaMgBr_3$ due to reduced lattice rigidity. In $NaMgCl_3$, Zn^{2+} shows the strongest preference for Na^+-site substitution (−13.90 eV per dopant), generating charge-compensating Na^+ vacancies. Ca^{2+} and Sr^{2+} also prefer Na^+-site, but with weaker driving forces. Trivalent dopants (Al^{3+}, Ga^{3+}) exhibit very strong substitution energies at Na^+-sites (−36.88 and −32.87 eV per dopant,

Table 2 Calculated formation energies (eV) of intrinsic defects, Schottky and Frenkel, and di/trivalent substitution mechanisms in $NaMgCl_3$ (NMC) and $NaMgBr_3$ (NMB) structures

Basic defects and lattice energy

	E_{vac}^{Na}	E_{vac}^{Mg}	E_{vac}^{X}	$E_{L}^{NaMgX_3}$	$E_{L}^{MgX_2}$	E_{L}^{NaX}	E_{L}^{LiX}
NMC	4.54	21.81	4.98	−69.08	−26.52	−8.09	−8.59
NMB	5.23	17.45	4.29	−58.29	−21.38	−7.59	−8.10

Basic defects and lattice energy

	E_{inter}^{Na}	E_{inter}^{Li}	E_{Na}^{Li}	E_{Mg}^{Li}	E_{Mg}^{Na}
NMC	−3.17	−3.85	−0.4	14.82	15.47
NMB	−3.71	−4.28	−0.41	10.91	11.40

	Schottky			Solution energy				
	Eqn (2b)	Eqn (3b)	Eqn (4b)	Eqn (5b)	Eqn (5d)	Eqn (6b)	Eqn (7b)	Eqn (8b)
NMC	−9.27	0.71	2.62	0.69	0.34	0.10	0.93	1.01
NMB	−7.58	0.96	2.32	0.76	0.48	0.09	0.96	0.95

		Divalent dopant (M^{2+})			Trivalent dopant (A^{3+})		
IR (Å)		0.74	1.00	1.18		0.54	0.62
Anion		Zn^{2+}	Ca^{2+}	Sr^{2+}		Al^{3+}	Ga^{3+}
Cl^-	$E_L^{MX_2}$	−26.93	−21.15	−21.14	$E_L^{AX_3}$	−55.85	−51.61
Br^-		−24.17	−20.16	−17.23		−50.68	−49.90
NMC	$E_{subs,Na}^{M^{2+}}$	−13.90	−8.56	−8.30	$E_{subs,Na}^{A^{3+}}$	−36.88	−32.87
NMB		−12.41	−9.02	−5.38		−21.03	−33.32
NMC	$E_{subs,Mg}^{M^{2+}}$	−0.87	6.03	6.46	$E_{subs,Mg}^{A^{3+}}$	−24.83	−20.64
NMB		−3.09	1.60	5.59		−12.36	−21.67

Solution energy (eV per defect)

NMC	Eqn (9b)	−0.23	0.33	0.54	Eqn (11b)	3.78	3.54
NMB		−0.30	0.38	1.44		5.78	1.42
NMC	Eqn (10b)	1.39	0.95	1.20	Eqn (12b)	3.01	3.00
NMB		1.80	1.19	1.90		4.86	1.50

respectively), but positive solution energies (3.0–3.8 eV per dopant) limit equilibrium incorporation. In $NaMgBr_3$, the softer lattice reduces solution energies, making aliovalent doping more accessible and amplifying vacancy generation. The above comparative analysis shows that $NaMgBr_3$, with its expanded and more deformable lattice, offers lower defect formation energies, enhanced mobility, and easier decomposition into Na_6MgBr_8 and $MgBr_2$ relative to $NaMgCl_3$. Both compounds favour Na^+ and halide vacancies, but $NaMgBr_3$ provides a more favourable environment for Frenkel defects, interstitial carriers, and aliovalent doping. Both Li^+ incorporations at Na^+-site and Zn^{2+} doping emerge as the most effective strategies in both halides, with $NaMgBr_3$ expected to deliver superior conductivity due to reduced migration barriers and softer lattice dynamics.

These results establish that while $NaMgCl_3$ is structurally robust but prone to decomposition into Na_6MgCl_8 and $MgCl_2$, $NaMgBr_3$ benefits from a softer lattice that lowers defect formation energies and may decompose into Na_6MgBr_8 and $MgBr_2$. The decomposition pathway provides important insight into the role of $NaMgX_3$ as a solid electrolyte interphase; because Na_6MgCl_8 has already been proposed in the literature as a promising SSE.[33]

This confirms that $NaMgX_3$, even if not the final conducting phase, can act as a precursor or stabilizing interfacial material whose decomposition products contribute directly to ionic transport and interfacial compatibility in sodium-ion batteries. The bromide analogue follows the same thermodynamic logic. $NaMgBr_3$ decomposes mirroring the chloride case. While Na_6MgBr_8 has not yet been investigated, its structural analogy to Na_6MgCl_8 suggests that it could also serve as a viable SSE candidate.[33] This parallel decomposition pathway strengthens the argument that $NaMgBr_3$, with its softer lattice and lower defect formation energies, may be even more effective as an SEI material.

3.3. Mechanical properties of $NaMgX_3$ structures

Mechanical stability of a battery material is of the vital importance to ensure good contact between electrodes and the electrolyte.[6,61–65] Magnitudes such as bulk, shear, and Young's modulus, including elastic anisotropy variables, are crucial for the appreciation of resistance to mechanical degradation and

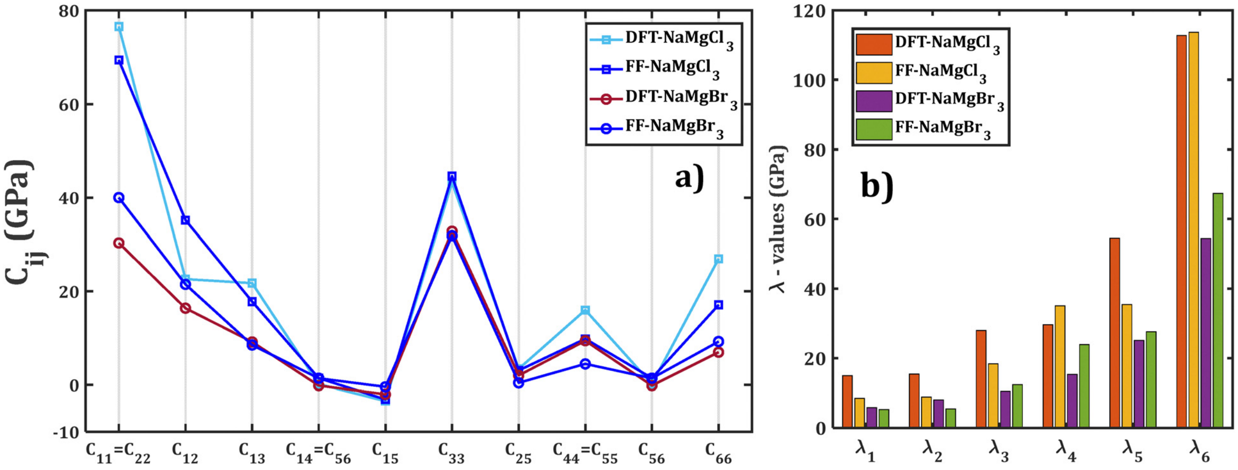

Fig. 3 (a) Elastic constant matrix elements (C_{ij}) and (b) eigenvalues of $NaMgX_3$ structures derived from DFT and FF geometry optimization computations.

malleability of the material, ensuring good contact with the electrodes/electrolyte (avoiding void formation responsible for parasitic currents) and insignificant volume expansion during the charge/discharge process. These desirable responses ensure the durability of the battery.[61–72]

Mechanical behaviour of a material is described by Hooke's law, specifically by the elastic stiffness tensor (C_{ij}) to elucidate the compliance with the Born stability criteria.[61] The computed C_{ij} matrix of $NaMgCl_3$ and $NaMgBr_3$ is given in Fig. 3a. The eigenvalues of the C_{ij} tensor provide some information concerning the principal modes of mechanical response within the crystal.[61–72] Each eigenvalue corresponds to a distinct deformation pathway, representing the resistance to strain along a specific combination of stress directions of the material.[61–72] A global mechanical stability is that the C_{ij}-eigenvalues must be positive.[61–72]

Fig. 3b shows the calculated eigenvalues of each compound. The corresponding C_{ij}-values are included in the SI file. All the eigenvalues are positive confirm mechanical stability of $NaMgX_3$ compounds. The dispersion in λ-magnitude reveals elastic anisotropy, where the lowest eigenvalues are associated with shear or compliant deformation modes, and the highest values reflect stiffer responses to axial tension or compression. This distribution suggests that $NaMgX_3$ compounds exhibit directional-dependent mechanical behaviour with direct implications on structural conformation under the action of an external stress.[61–72] The negative value of C_{15} and C_{24} suggests a non-trivial coupling between normal strains along the x- and y- directions, due to anisotropic interatomic interactions or structural relaxation mechanisms.

Other mechanical properties are derived from the compliance matrix ($S_{ij} = C_{ij}{}^{-1}$). To evaluate the macroscopic mechanical properties of $NaMgX_3$ structures, elastic moduli and related metrics are computed. The resistance to deformation and volume change are described by the bulk and shear modulus.[61–72] Under the Voigt approximation, a uniform strain on the lattice structure is assumed.[61] The Reuss approximation assumes a uniform stress on the lattice structure,[65] where the shear and bulk modulus are computed from S_{ij}, while the Hill approximation combines both the Voigt and Reuss approaches.[66,67] Explicit formulation of each approximation, including the Young modulus, is described elsewhere.[61–63]

A percentage of anisotropy regarding compressibility (A_B) and shear (A_G) for nanocrystalline samples, including the universal anisotropy (A^U), is defined by eqn (17):[68]

$$\begin{aligned} A_B &= \frac{B_{\text{Voigt}} - B_{\text{Reuss}}}{B_{\text{Voigt}} + B_{\text{Reuss}}}; \\ A_G &= \frac{G_{\text{Voigt}} - G_{\text{Reuss}}}{G_{\text{Voigt}} + G_{\text{Reuss}}}; \\ A^U &= 5\left(G_{\text{Voigt}}/G_{\text{Reuss}}\right) + \left(B_{\text{Voigt}}/B_{\text{Reuss}}\right) - 6 \end{aligned} \tag{17}$$

When the A_B, A_G and A^U values trend to zero, the structure exhibits elastic isotropy and is anisotropic when their values amount to a near 1.[68] The Kleinman coefficient (K) measures the internal contraction stability of a material, disclosing the resistance to both stretching and bending, including the ability to withstand external forces maintaining the structural framework.[69]

The machinability index ($M = B/C_{44}$) is a useful metric regarding industrial and commercial applications of a material.[70,71] When the machinability index exceeds a value of 1.45, the compound is considered as suitable for manufacturing.[70,71] Relevant characteristics such as hardness, machine tool durability, cutting form and operational capacity can be assembled about the machinability of materials.[70,71] This factor helps determine the overall effectiveness of machining processes for the SEI.[70,71]

Macroscopic elastic properties of $NaMgCl_3$ and $NaMgBr_3$ are summarized in Table 3. For $NaMgCl_3$, the Hill-averaged bulk modulus (B) is 34.5 GPa from FF and 35.2 GPa from DFT computations, showing a close agreement and confirming the chloride's relatively high stiffness. In contrast, $NaMgBr_3$ exhibits a much lower B value, with FF predicting 20.4 GPa and DFT 18.1 GPa. Both methods consistently indicate that the chloride

Table 3 Macroscopic mechanical properties of $NaMgX_3$ compounds, derived from DFT and FF computations. Bulk modulus (B), shear modulus (G), Young's modulus (E), and Pugh's ratio (B/G) are reported using Reuss, Voigt, and Hill averaging schemes. Additional indicators include the machinability index (M), anisotropy factors (A_B and A_G), compressibility (β), Kleinman parameter (K), and universal anisotropy index (A^U)

	$NaMgCl_3$						$NaMgBr_3$					
	FF			DFT			FF			DFT		
Parameters	Reuss	Voigt	Hill	Reuss	Voigt	Hill	Reuss	Voigt	Hill	Reuss	Voigt	Hill
B (GPa)	32.88	36.10	34.49	33.88	36.51	35.20	19.9	20.99	20.44	18.03	18.10	18.07
G (GPa)	12.56	14.85	13.70	18.49	20.47	19.48	6.50	8.53	7.51	8.18	9.08	8.63
E (GPa)	47.10	47.10	38.51	46.93	51.73	49.33	26.84	26.84	29.48	21.32	23.34	22.34
B/G	2.62	2.43	2.52	1.83	1.78	1.81	3.06	2.46	2.72	2.20	1.99	2.09
M	3.35	3.68	3.52	2.12	2.28	2.20	4.46	4.70	4.58	1.91	1.92	1.92
A_B	0.05			0.04			0.03			0.002		
A_G	0.08			0.05			0.14			0.052		
β (GPa^{-1})	0.03			0.03			0.05			0.06		
K	0.63			0.44			0.66			0.66		
Au	1.01			0.61			1.62			0.55		

phase is substantially less compressible than the bromide analogue, in line with the Hill-averaged compressibility values of 0.03 GPa^{-1} (both FF and DFT) for $NaMgCl_3$ *versus* 0.05 GPa^{-1} for $NaMgBr_3$.

The shear modulus (G) and Young's modulus (E) highlight the stronger mechanical robustness of $NaMgCl_3$. FF yields Hill-averaged G = 13.7 GPa and E = 38.5 GPa, while DFT gives higher values of G = 19.5 GPa and E = 49.3 GPa. For $NaMgBr_3$, FF predicts G = 7.5 GPa and E = 29.5 GPa, whereas DFT returns G = 8.6 GPa and E = 22.3 GPa. Thus, both methods agree on the relative trend, that is, $NaMgCl_3$ is stiffer and stronger than $NaMgBr_3$, but DFT values consistently provide more conservative (higher) estimates for the chloride and slightly lower values for the bromide.

The Pugh's ratio (B/G) further differentiates the two halides. For $NaMgCl_3$, FF gives B/G = 2.5 while DFT yields 1.8, placing the chloride closer to the brittle–ductile boundary in the DFT description. For $NaMgBr_3$, FF predicts B/G = 2.7 and DFT 2.1, both indicating ductility but with DFT again moderating the extent. These results confirm that $NaMgCl_3$ is stiffer and less compressible, while $NaMgBr_3$ is softer and more ductile, supporting their proposition as a candidate SEI.

The machinability index (M) also reflects this contrast. For $NaMgCl_3$, FF gives M = 3.5 and DFT 2.2, while for $NaMgBr_3$ FF yields 4.6 and DFT 1.9. Both methods suggest a mechanical processability; elastic anisotropy remains low in both compounds: for $NaMgCl_3$, FF reports A_B = 0.05 and A_G = 0.08, while DFT gives A_B = 0.04 and A_G = 0.05.

For $NaMgBr_3$, FF yields A_B = 0.03 and A_G = 0.14, while DFT results in similar values. The universal anisotropy index (A^U) is 1.01 (FF) *versus* 0.61 (DFT) for $NaMgCl_3$, and 1.62 (FF) *versus* 0.55 (DFT) for $NaMgBr_3$. These consistently low values from both methods indicate that both halides are nearly elastically isotropic, which is an advantageous feature for polycrystalline processing and interfacial mechanical stability.

As a complement to the mechanical stability, the anisotropic behaviour of the elastic moduli is evaluated. The directional dependence of both Young's modulus (E) and shear modulus (G) is shown in Fig. S1 for $NaMgCl_3$ and $NaMgBr_3$ structures.

The three-dimensional plots reveal that neither compound exhibits isotropic elasticity, with $NaMgCl_3$ showing stronger directional variations in E, whereas $NaMgBr_3$ displays comparatively smoother anisotropy in G. These results highlight how halide substitution (Br^- by Cl^-) modifies the elastic response, providing insight into the mechanical robustness of these materials under different stress orientations.

The Kleinman parameter (K) provides us with additional insights into bond flexibility.[69] For $NaMgCl_3$, FF yields K = 0.63 while DFT gives a lower value of 0.44, suggesting that the FF description emphasizes bond bending more strongly than DFT. For $NaMgBr_3$, FF predicts K = 0.66 and DFT returns 0.55, again showing that both methods agree with each other on the relative trend, bond bending plays a slightly greater role in the bromide lattice, but FF consistently produces higher values. This divergence underscores the different bonding environments in both halides and highlights how methodological choice can shift the quantitative estimate of bond flexibility.

It is important to emphasize that $NaMgBr_3$ has not been reported experimentally yet. Further experimental confirmation is required to validate these predictions. Exploration of interfacial material properties in this study represents a predictive design task, where both DFT and FF simulations are used in tandem to assess feasibility and potential roles as SEI. The consistent qualitative agreement between both methods strengthens confidence in the physical trends, while the quantitative differences provide transparent bounds on uncertainty.

In the present study, we propose both $NaMgCl_3$ and $NaMgBr_3$ as candidate components of the SEI. Their ductility, low elastic anisotropy, and balanced bonding contributions that are similar to those of other battery materials,[7,33,43,44,73] suggest that they could accommodate interfacial stresses without catastrophic fracture. The chloride phase, with its higher stiffness and lower compressibility, may provide enhanced resistance to densification under stack pressure, while the bromide analogue, though softer, could offer improved compliance at electrode interphases. These complementary traits highlight the potential of both halides as mechanically stable SEI constituents, bridging robustness and adaptability in sodium-based batteries.

3.4. Na transport properties of $NaMgX_3$ structures

Fig. 4 depicts the energy landscape for Na^+ migration in $NaMgX_3$ ($X = Cl^-$, Br^-). Under the BVSE approach, the relaxed crystal structure is sampled on a fine 3D grid of fractional coordinates and the local site energy for the Na^+ ion is evaluated at each grid point based on bond-valence interactions; the resulting scalar field was rendered as translucent isosurfaces to highlight low-energy regions.[39,40,58] This representation emphasizes both the preferred occupancy sites and the percolation topology for Na^+ transport, allowing a direct comparison between the Cl^- and Br^- anion variants in terms of pathway connectivity and relative site energies.

The isosurfaces correspond to regions of low site energy, identifying conduction channels where Na^+ ions can move most favourably. Green spheres mark the equilibrium Na^+ positions, while the crystallographic axes provide orientation. In $NaMgCl_3$ (Fig. 4a and c), the conduction channels are present but relatively constrained, with higher energy bottlenecks limiting connectivity between sites. In contrast, $NaMgBr_3$ (Fig. 4b and d) contains a more open and interconnected three-dimensional network, where Na^+ ions can move along multiple crystallographic directions with smoother connectivity and lower saddle points. This dimensionality of the migration path is a key distinction: while both halides support Na^+ transport, the bromide phase provides a genuinely three-dimensional conduction network, which reduces anisotropy and enhances long-range ionic mobility. The BVSE maps therefore demonstrate that halide identity not only influences barrier heights but also the dimensionality of Na^+ migration, with Br^- substitution enabling a more efficient 3D conduction topology.

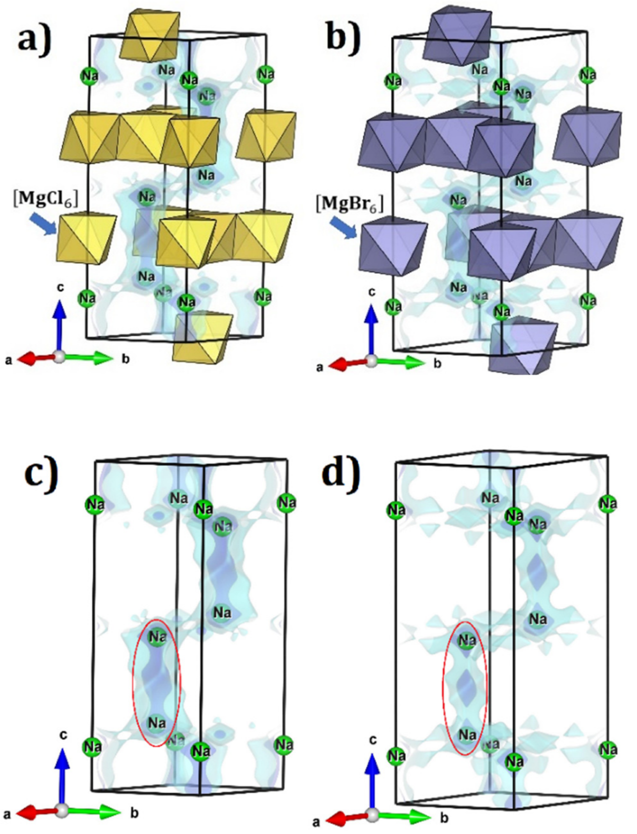

Fig. 4 Energy landscape for Na^+ migration in optimized $NaMgX_3$ ($X = Cl^-$, Br^-). (a) and (b) Blue isosurfaces show low energy pathways in $NaMgCl_3$ and $NaMgBr_3$; $[MgX_6]$ octahedra are shown. (c) and (d) Red ellipses highlight contiguous channels. Darker/denser isosurfaces denote energy minima and lighter/absent regions denote higher energy barriers.

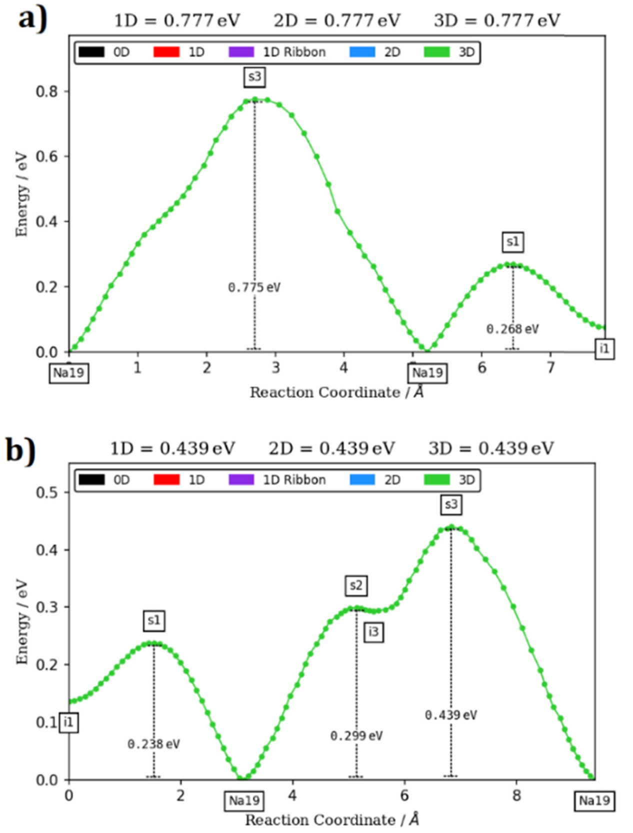

Fig. 5 Energy *versus* reaction coordinate of optimized $NaMgX_3$ structures: (a) $NaMgCl_3$ and (b) $NaMgBr_3$.

Fig. 5 shows the energy profiles along the Na^+ migration pathways in $NaMgCl_3$ and $NaMgBr_3$, derived from BVSE analysis of FF optimized structures. In $NaMgCl_3$, the migration path follows a relatively simple sequence of Na^+-site (Na) – saddle point (s) – Na^+-site (Na) – interstitial (i).

Transport is thus constrained, with a determinant energy barrier of 0.78 eV across all directions, and limited flexibility in connecting stable Na^+ sites through intermediate positions. In contrast, $NaMgBr_3$ exhibits a more complex and extended three-dimensional migration sequence of i–s–Na–s–i–s–Na. The energy landscape in this case is smoother, with multiple saddle points ranging from 0.24 to 0.44 eV, and interstitial positions that are energetically more accessible. This richer conduction topology reflects the larger and more polarizable bromide anion, which expands the lattice and lowers migration barriers.

The comparison underscores a fundamental difference in conduction topology. While $NaMgCl_3$ supports Na^+ transport through a restricted pathway, $NaMgBr_3$ genuinely supports a

Table 4 Surface energies (γ), activation energies ($E_a{}^{\sigma}$), and room-temperature (300 K) conductivities (σ_0) of $NaMgX_3$ for selected crystallographic orientations and bulk structures

	$NaMgCl_3$			$NaMgBr_3$		
Type	γ (J m^{-2})	$E_a{}^{\sigma}$ (eV)	σ_0 (S cm^{-1})	γ (J m^{-2})	$E_a{}^{\sigma}$ (eV)	σ_0 (S cm^{-1})
100	4.96	0.06	1.24×10^{-1}	3.99	0.19	1.19×10^{-3}
001	0.29	0.43	1.76×10^{-7}	2.51		
011	0.39			0.26		
111	0.43			0.15	0.41	4.02×10^{-8}
210	0.45			0.20		
Bulk		0.75	7.55×10^{-12}		0.41	2.05×10^{-6}

truly 3D network of interconnected sites and hops. In $NaMgCl_3$, the high, direction-invariant barrier restricts the number of viable transitions between stable Na^+ positions, increasing the likelihood of bottlenecks and making long-range transport highly sensitive to local disorder or blocking defects. In contrast, $NaMgBr_3$ with more distributed saddle points creates multiple accessible interstitial sites and alternative routes; with the enhanced diffusivity and conductivity reported in Table 4, which will be discussed in a following section.

Fig. 6 and Table S1 (SI file) together provide a macroscopic view of Na^+ transport in $NaMgX_3$ structures. The Arrhenius plots demonstrate the thermally activated nature of diffusion and conductivity, with linear trends confirming hopping between lattice sites as the dominant mechanism. Differences in slope between chloride and bromide frameworks reflect the distinct energy landscapes described above. $NaMgCl_3$ shows steeper profiles consistent with more constrained pathways and pronounced bottlenecks, while $NaMgBr_3$ exhibits gentler slopes indicative of smoother conduction channels and reduced barriers.

Table S1 complements these plots by summarizing the relative transport coefficients and conductivities, highlighting the systematic influence of halide substitution and computational method. Together, these results establish a direct correlation between the microscopic migration paths (Na–*i*–*s*–Na) observed in BVSE energy profiles and the macroscopic transport properties, underscoring the defect-tunable nature of Na^+ conduction in $NaMgX_3$ structures.

Within the sodium halides, both Na_2MgCl_4 and Na_2ZnCl_4 also show efficient transport behaviour, with small activation energies of 0.17–0.18 eV and conductivities in the 10^{-4} S cm^{-1} range.[71] The bromide counterpart $NaAlBr_4$ stands out with an ultra-small activation energy of 0.10 eV and a conductivity of 0.11 S cm^{-1}, thus surpassing most chloride analogues.[21] In contrast, extended stoichiometries display limited transport due to higher activation barriers (0.39–0.56 eV) and conductivities below 10^{-6} S cm^{-1}.[73] These findings emphasize that ionic conductivity is strongly influenced by both defect chemistry and migration energetics. Lower defect formation energies promote the creation of mobile charge carriers, while reduced migration barriers allow their rapid movement through the lattice. The combination of these effects leads to a marked improvement in conductivity. Bromide substitution serves as a decisive structural modification, alleviating chloride-induced bottlenecks and producing a more open and interconnected percolation network. More broadly, targeted anion substitution offers a rational approach to improve ion mobility and advance solid-state conductors. The Na^+ transport properties of $NaMgX_3$ emerge from the close interplay between lattice structure, defect chemistry, and migration energetics. BVSE maps (Fig. 4) reveal three-dimensional conduction networks punctuated by bottlenecks, while the energy profiles (Fig. 5) trace the migration path from Na lattice sites through interstitial positions and across saddle points, highlighting how halide substitution modulates barrier heights and pathway connectivity.

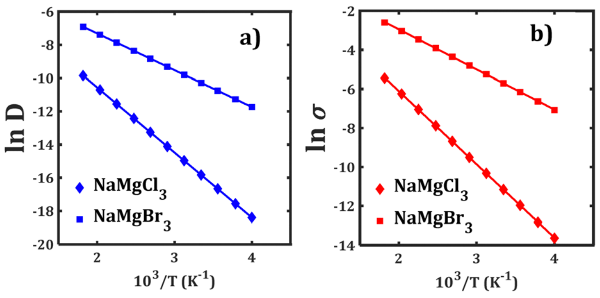

Fig. 6 Linear Arrhenius dependence of Na^+-ions: (a) diffusion coefficient (D), and (b) conductivity (σ) in $NaMgX_3$ structures.

The most probable intrinsic defect is the NaX Schottky pair, which promotes the formation of Na^+ vacancies and thereby enhances carrier density. Structural descriptors of the $[MgX_6]$ octahedra (including V, L, Ω, d_i, Q, and ECN collected in Table 1) confirm that lattice distortions and polyhedral flexibility strongly influence the topology of conduction channels. These microscopic features translate into the Arrhenius-type trends observed in Fig. 6, where differences in slope reflect the relative ease of ion hopping in chloride *versus* bromide frameworks. Table S consolidates these results, showing systematic variations in diffusion and conductivity that align with halide identity, lattice distortion, and defect chemistry. Together, these analyses establish a direct correlation between atomic-scale migration pathways and bulk transport properties, underscoring the defect tunable nature of Na^+ conduction in $NaMgX_3$ halides.

3.5. Surface stability and its transport properties

The constructed surfaces of $NaMgX_3$ structures are given in Fig. S2. Table 4 lists the results of the surface energy (γ) of $NaMgX_3$ structures. Due to the trigonal symmetry of $R\bar{3}$, several surfaces are symmetrically equivalent. Specifically, (100) and (010) belong to the same family, as do (011) and (110). Consequently, only four unique orientations (100), (011), (001), (111), and (210) are considered. The slab calculations highlight the anisotropy in surface stability for both compounds. In $NaMgCl_3$, the (001) orientation exhibits the lowest surface energy (0.29 J m^{-2} per side), making it the most stable surface and the one most likely to dominate in crystal growth or interphase formation. In contrast, the (100) orientation shows much higher value (4.96 J m^{-2}), indicating reduced stability. Intermediate stabilities

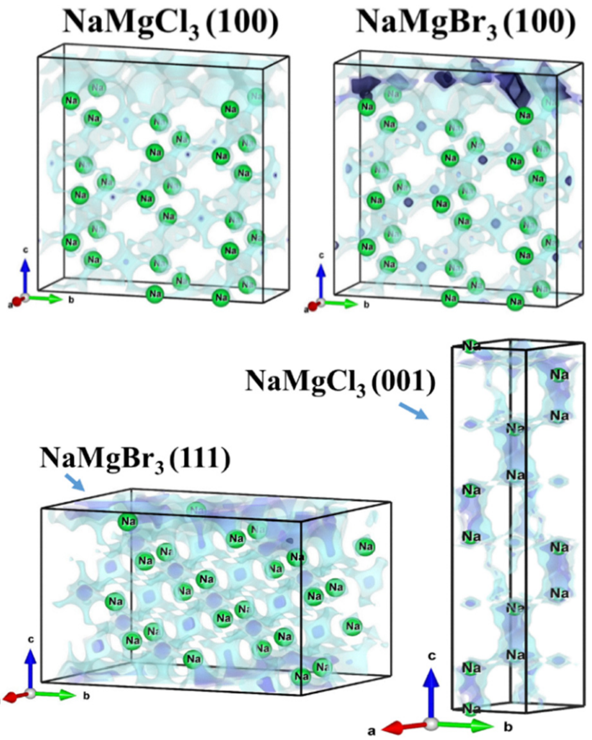

Fig. 7 Energy landscape (blue isosurfaces) of the most stable and unstable $NaMgX_3$ surfaces, highlighting conduction channels. Darker/denser isosurfaces denote energy minima and lighter/absent regions denote higher-energy barriers.

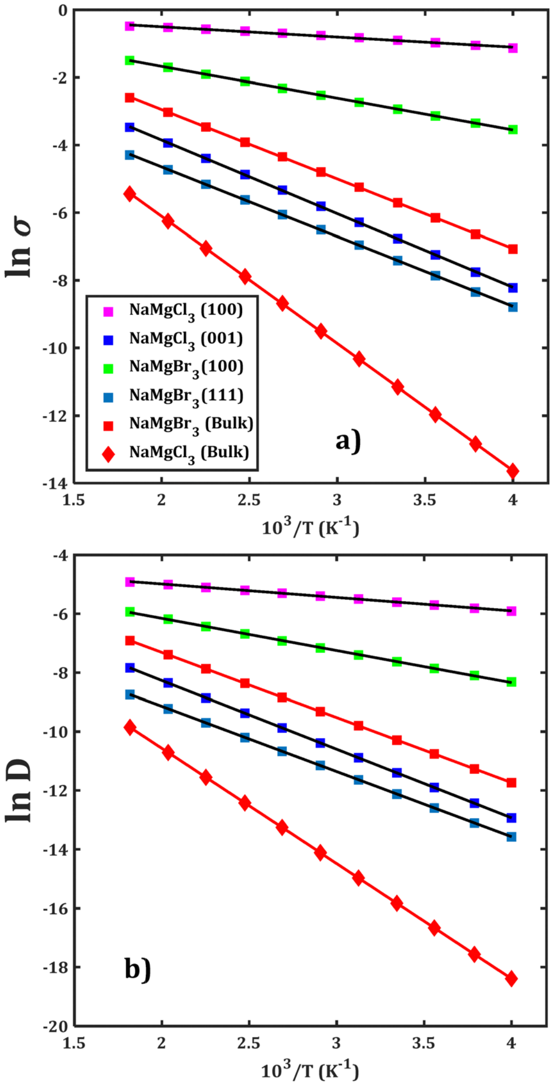

Fig. 8 Arrhenius-type dependence of Na^+-ion: (a) conductivity (σ), and (b) diffusion coefficient (D) of $NaMgX_3$ surface structures. Plots of bulk structures are included for comparison.

are observed for the (011) and (111) orientations, with energies between 0.39–0.43 J m^{-2}.

For $NaMgBr_3$, the (111) orientation is the most stable, with a surface energy of 0.15 J m^{-2} per side, followed by the (210) direction (~0.20 J m^{-2}). The (011) orientation also shows low energy of 0.26 J m^{-2}, while the (100) and (001) orientations are significantly higher (3.99 and 2.51 J m^{-2}, respectively). This contrast underscores a key difference between the chloride and bromide systems, where $NaMgCl_3$ favours the (001) surface, whereas $NaMgBr_3$ stabilizes the (111) orientation. These findings emphasize the role of halide chemistry in determining surface anisotropy. The lowest-energy surfaces identified here suggest preferential cleavage planes and potential pathways for defect formation. The values of surface energy are comparable to those of other studies previously reported in the literature.[74–77] Such insights are directly relevant to correlating surface stability with mechanical properties, elastic moduli, and reactivity trends, and they provide a foundation for linking surface energetics with defect-driven transport mechanisms.

To explore the transport properties of these surfaces, we now apply BVSE computations to extract activation energies and room-temperature conductivities, following the same methodology used for bulk $NaMgBr_3$ and $NaMgCl_3$ compounds. To our knowledge, studies applying BVSE computation on surfaces have not been reported yet.

To avoid redundancy, we disclose only the transport properties of the most stable and unstable surfaces in each system, since these represent the two extremes of interfacial behaviour. In this sense, the comparison highlights a counterintuitive but reproducible trend, that is, while the most stable surfaces exhibit poor Na^+ transport due to their rigid, defect-suppressing environments, the most unstable surfaces consistently show enhanced conductivity and reduced migration barriers. This arises from an under-coordination of surface ions, the ease of Na^+ vacancy formation, and the electrostatic asymmetry inherent to high-energy terminations. Thus, the surface instability revealed from BVSE analysis, although energetically unfavourable, can act as a transport accelerator, providing efficient Na^+ pathways that are absent in the bulk-like stable facets. This duality underscores the importance of considering both stability and transport characteristics when evaluating halide solid electrolytes, as the balance between these properties ultimately governs the interfacial performance in solid-state Na batteries.

Fig. 7 shows the energy landscape of the most stable and unstable $NaMgX_3$ surfaces, while Fig. S3 (SI file) shows their NEB profiles. A clear distinction emerges between $NaMgCl_3$ and $NaMgBr_3$ in terms of the relationship between bulk and surface transport properties. For $NaMgCl_3$, the most stable surface (*e.g.*, the (001)) preserves the bulk-like octahedral environment, resulting in an energy landscape which closely mirrors those of the bulk (see Fig. 4a). Because the migration energy barriers and conduction pathways remain essentially unchanged, the Na^+ transport at the interphase is predictable from bulk energetics. This convergence underscores the structural rigidity of the $[MgCl_6]$ octahedra and the robustness of the Cl^- framework, which together ensure isotropic conduction even under interfacial conditions.

In contrast, $NaMgBr_3$ brings in a significant divergence between bulk and surface BVSE landscapes. The expanded $[MgBr_6]$ octahedra, with larger volumes and longer Mg–Br bond lengths (see Table 1), introduce enhanced lattice softness and polarizability.

At Br-rich surface terminations, relaxation effects alter local site energies and defect stabilization, leading to anisotropic transport pathways. Migration energy barriers, seen in BVSE maps, vary across facets, with certain surfaces acting as preferential conduction channels while others impose bottlenecks. This facet-dependent behaviour highlights the sensitivity of $NaMgBr_3$ to interfacial conditions and suggests that its ionic conductivity cannot be inferred solely from bulk energetics.

Accordingly, $NaMgCl_3$ maintains bulk-like transport behaviour even at its most stable surface, while $NaMgBr_3$ exhibits surface-modulated conduction with pronounced anisotropy. This contrast emphasizes the decisive role of halide identity in governing interfacial transport properties, with Cl^- anion frameworks offering predictable bulk-to-surface continuity and Br^- anion frameworks introducing variability that must be explicitly considered in the solid-state electrolyte design.

Fig. 8 shows the Arrhenius-type dependence of the most stable and unstable $NaMgX_3$ surfaces. From an Arrhenius-type fit, their transport properties are derived and included in Table 4.

Together with surface energies, Table 4 lists computed activation energies ($E_a{}^{\sigma}$) and room-temperature conductivities (σ_0) for selected facets and bulk $NaMgCl_3$ and $NaMgBr_3$ surfaces along bulk transport properties; all these results suggest a strong facet dependence of Na^+ transport. For $NaMgCl_3$ the high-energy (100) termination is associated with an exceptionally small energy barrier of 0.06 eV and very high conductivity of 124 mS cm^{-1}, while the (001) termination already shows substantially enhanced transport relative to the bulk counterpart. Similarly, the Li_3OCl (100) antiperovskite structure implies a Li energy barrier of only 0.08 eV derived from nudged elastic band computations.[74] In $NaMgBr_3$ the most stable surface (111) has an activation energy similar to the bulk, but a lower conductivity of two orders of magnitude, whereas the unstable (100) surface produces a moderate barrier reduction of 0.19 eV and increased conductivity of 1.19 mS cm^{-1}.

Of the two compounds, $NaMgBr_3$ offers the best balance between transport and surface properties. Its bulk conductivity is several orders of magnitude higher than that of bulk $NaMgCl_3$, and its surface energies are generally lower, indicating more stable terminations; the (100) facet provides a useful conductivity enhancement without the extreme surface energy and reactivity associated with $NaMgCl_3$ (100). By contrast, $NaMgCl_3$ delivers the highest absolute surface conductivities at unstable facets but at the cost of very high surface energy (greater chemical reactivity and likely interphase formation), which complicates interphase stability. Therefore, for realistic solid-state electrolyte applications where a compromise between low interfacial resistance and manageable surface reactivity is required, $NaMgBr_3$ is the more effective candidate to be considered; $NaMgCl_3$ can still be attractive where engineered coatings or interlayers can stabilize high-energy, high-conductivity facets.

4. Concluding remarks

In the present theoretical study, advanced atomistic simulations are combined to deliver a quantitative, property-level comparison of the known $NaMgCl_3$ and predicted $NaMgBr_3$ compounds. The optimized lattice parameters highlight the methodological spread: for $NaMgCl_3$, FF yields $a = b = 6.289$ Å and $c = 18.339$ Å, while DFT gives slightly larger values of $a = b = 6.425$ Å and $c = 19.401$ Å. For $NaMgBr_3$, FF predicts a pronounced in-plane expansion with $a = b = 7.423$ Å and $c = 20.537$ Å, whereas DFT provides a more moderate estimate of $a = b = 6.855$ Å and $c = 20.935$ Å.

The larger ionic radius and polarizability of the Br^- anion produce a softer, more deformable bromide lattice (lower bond-angle variance, higher distortion index) that opens expanded conduction channels and reduces energetic penalties for ionic motion. Treatment of both series of FF and DFT results as paired bounds provides a conservative estimate of structural uncertainty and reinforces confidence in the predictive framework for SEI design. DFT calculations yield band gaps of 5.0 eV for $NaMgCl_3$ and 3.7 eV for $NaMgBr_3$, confirming their electronically insulating character.

Across both DFT and FF approaches, the mechanical metrics consistently quantify SEI-relevant resilience: $NaMgCl_3$ emerges as noticeably stiffer than $NaMgBr_3$ in bulk, shear, and Young's moduli, while both halides remain within the ductile regime. FF tends to overestimate ductility and machinability, whereas DFT provides more conservative upper and lower bounds, yet both methods agree that elastic anisotropy is low. These properties indicate that each compound can accommodate interfacial stress and stack pressure without catastrophic fracture, reinforcing their suitability as mechanically compatible SEI constituents in sodium batteries.

Defect energetics are dominated by a small set of mechanisms that control carrier concentration and interfacial chemistry: Na–X Schottky formation, Na^+ Frenkel and Li^+ interstitial disorder, and aliovalent substitution *via* divalent and trivalent dopants. The calculations show accessible Frenkel and substitutional pathways (Na^+ Frenkel ∼0.69 eV/0.76 eV; Li^+ interstitial ∼0.34 eV/0.48 eV; Li^+ substituting at Na^+-site ∼0.10 eV/0.09 eV for $NaMgCl_3$ and $NaMgBr_3$, respectively), indicating practical, low-energy routes to increase mobile carrier concentration.

Of the aliovalent strategies, a divalent substitution at Na sites is the most realistic vacancy-generating mechanism, namely, Zn^{2+} emerges as the preferential divalent dopant with the strongest Na^+-site preference and favourable substitution energetics, while Ca^{2+} and Sr^{2+} are viable but weaker alternatives. Trivalent dopants (Al^{3+} and Ga^{3+}) bind strongly to lattice sites but exhibit positive solution energies that limit equilibrium incorporation, so their effective use requires non-equilibrium syntheses or tightly controlled chemical potentials.

Decomposition appears naturally within the defect-thermodynamic landscape in such a way that full-Schottky energetics connect $NaMgX_3$ to ternary reorganization products (Na_6MgX_8 + MgX_2). Because Na_6MgCl_8 has been proposed as a sodium conductor, these pathways reframe $NaMgX_3$ phases as SEI precursors whose controlled or partial reorganization can yield electrochemically relevant, conducting interphases rather than purely deleterious decomposition products. The bromide analogue, with its softer lattice and lower defect formation energies, is predicted to be particularly effective at seeding conductive interphases; Na_6MgBr_8 therefore merits experimental evaluation as a potential solid electrolyte.

Transport and surface analyses provide us with the practical picture for interfacial performance. Bulk metrics show that Br^- substitution lowers migration barriers and raises intrinsic conductivity (bulk activation energies of 0.75 eV for $NaMgCl_3$ *versus* 0.41 eV for the $NaMgBr_3$, with corresponding conductivities of 7.6×10^{-12} and 2.1×10^{-6} S cm^{-1} at 300 K). Surface energetics are strongly facet-dependent, the lowest-energy facets are (001) for $NaMgCl_3$ and (111) for $NaMgBr_3$ (surface energies of 0.29 and 0.15 J m^{-2}, respectively), while high-energy terminations such as (100) are much less stable (surface energies of 4.0–5.0 J m^{-2}). High-energy surfaces produce the lowest migration energy barriers and the highest surface conductivities, whereas the most stable facets are far less conductive. These values quantify the stability-transport trade-off and the facet exposure must be controlled or passivated to exploit high-conductivity terminations without sacrificing chemical stability.

For practical implementation, we need to prioritize controlled Li^+ and Zn^{2+} doping at Na^+-site under Na-poor chemical potentials to raise carrier concentrations while minimizing uncontrolled ternary reorganization, to target the lowest-energy facets in device architectures ($NaMgCl_3$(001) and $NaMgBr_3$(111)) and to use selective facet exposure or thin protective coatings to access high-conductivity terminations safely.

In conclusion, while the chloride $NaMgCl_3$ is structurally robust and can produce extremely high surface conductivities at unstable facets, but requires a careful interfacial control, the bromide $NaMgBr_3$ counterpart combines lattice softness, lower bulk migration energy barriers and generally lower surface energies to offer a better compromise between interfacial stability and ionic transport for SEI applications.

The quantitative datasets that are predicted in this paper, including structural descriptors, defect energetics with explicit dopant preferences, elastic moduli, surface energies, activation barriers, and conductivities, all emphasize a concrete roadmap for experimental syntheses, facet engineering, and targeted doping to tune up the interphase performance and to intentionally harness a defect-driven reorganization as an open avenue to an efficient conductive SEI formation.

Conflicts of interest

There are no conflicts to declare.

Data availability

The data supporting this study are available from the corresponding author upon reasonable request.

Supplementary information: octahedral-geometry metrics; DFT and force-field elastic constants with anisotropy plots; predicted Na^+ diffusion and conductivity parameters and migration profiles; atomic surface views; and the full force-field parameter set for reproducibility. See DOI: https://doi.org/10.1039/d6cp01022a.

Acknowledgements

MTN and BNNH thank Van Lang University, Vietnam, for support.

References

1 X. Bi, W. Mu, J. Meng, Y. Huang, X. Lei, Q. Wang and S. Luo, *Energy Storage Mater.*, 2024, **73**, 103807.
2 M. Armand and J. M. Tarascon, *Nature*, 2008, **451**, 652–657.
3 Y. Zhang, R. Cao, C. Ouyang, L. Jiang, Y. Wang, M. Yang and H. Xia, *J. Mater. Chem. A*, 2025, **13**, 3973–3990.
4 M. M. Mashfy, T. A. Alvy, N. Hossain, M. A. Haque, F. T. Mohsin, T. Sharmin and M. Nasim, *Next Energy*, 2026, **10**, 100478.
5 S. A. Riza, R. Xu, Q. Liu, M. Hassan, Q. Yang, D. Mu, L. Li, F. Wu and R. Chen, *New Carbon Mater.*, 2024, **39**, 743–769.
6 D. J. Lee, Q. Yin, D. Xu and Z. Chen, *Chem. Rev.*, 2025, **125**, 9332–9381.
7 T. Yu, Y. Liu, H. Li, Y. Sun, S. Guo and H. Zhou, *Chem. Rev.*, 2025, **125**, 3595–3662.
8 T. Jeon, S. Park, D. H. Shin, G. Kim and S. C. Jung, *ACS Appl. Mater. Interfaces*, 2026, **18**, 5094–5103.
9 C. Wu, Z. Wang, Z. Jia, J. Cui, C. Shu, X. Wang, Y. Wu and W. Tang, *EES Batter.*, 2025, **1**, 364–384.
10 M. Wang, L. Deng, K. Wang, K. Zou, T. Yang, X. Liao, R. Xiao and X. Ke, *Electrochim. Acta*, 2026, 148454.
11 M. Li, C. Sun, R. Zhang, M. Qi, Z. Wu, X. Zhang, Y. Zhang, J. Yuan and N. Zhang, *Adv. Mater.*, 2025, **37**, e10882.

12 D. Wang, X. Wu, Y. Ren, Y. Li, X. Xie, X. Ma, I. Razanau, X. Chen, J. Lu and K. Pan, *Nanoscale Adv.*, 2025, **7**, 4535–4550.

13 A. M. Bogale, Y. A. Kumar, M. E. Suk, F. B. Tesema, M. M. Solomon, S. K. Jilcha and A. Y. Tiky, *J. Power Sources*, 2026, **663**, 238584.

14 E. Wang, S. Ge, W. Li, B. Fu, F. Zhou and W. Chen, *Matter*, 2025, **8**, 102368.

15 L. Huang and C. Huang, *Electrochem. Energy Rev.*, 2026, **9**, 6, DOI: 10.1007/s41918-026-00279-y.

16 Y. Zheng, S. Zhang, J. Ma, F. Sun, M. Osenberg, A. Hilger, H. Marktter, F. Wilde, I. Manke and Z. Hu, *Sci. Bull.*, 2023, **68**, 13.

17 A. Banerjee, X. Wang, C. Fang, E. A. Wu and Y. S. Meng, *Chem. Rev.*, 2020, **120**, 6878–6933.

18 X. Wang, W. Hou, Y. Chen, Y. Yang, Y. Wang, Z. Guo, Z. Song and Y. Liu, *Adv. Energy Mater.*, 2024, **15**, 2402731.

19 Z. Wang, J. Tan, Z. Jia, J. Cui, X. Wang, C. Shu, X. Gao, Y. Wu and W. Tang, *ACS Energy Lett.*, 2024, **9**, 4485–4492.

20 J. Liang, E. van der Maas, J. Luo, X. Li, N. Chen, K. R. Adair, W. Li, J. Li, Y. Hu, J. Liu, L. Zhang, S. Zhao, S. Lu, J. Wang, H. Huang, W. Zhao, S. Parnell, R. I. Smith, S. Ganapathy, M. Wagemaker and X. Sun, *Adv. Energy Mater.*, 2022, **12**, 2270085.

21 Y. Li, D. McCoy, J. Bordonaro, J. W. Simonson, S.-Y. Liu and S. Wang, *J. Phys.: Condens. Matter*, 2024, **36**, 445702.

22 Y. Kim and S. Choi, *J. Power Sources*, 2023, **567**, 232962.

23 Z. Huang, S. Yoshida, H. Akamatsu, K. Hayashi and S. Ohno, *ACS Mater. Lett.*, 2024, **6**, 1732–1738.

24 H. Kwak, J. Lyoo, J. Park, Y. Han, R. Asakura, A. Remhof, C. Battaglia, H. Kim, S. T. Hong and Y. S. Jung, *Energy Storage Mater.*, 2021, **37**, 47–54.

25 W. D. Richards, L. J. Miara, Y. Wang, J. C. Kim and G. Ceder, *Chem. Mater.*, 2016, **28**, 266–273.

26 L. Guo, J. Zheng, L. Zhao and Y. Yao, *MRS Bull.*, 2023, **48**, 1247–1256.

27 S.-Y. Lee, J. Rawal, J. Lee, J. Gautam, S. Kim, G.-L. Xu, K. Amine and S.-J. Park, *Electrochem. Energy Rev.*, 2025, **8**, 9.

28 A. C. C. Dutra, B. A. Goldmann, M. S. Islam and J. A. Dawson, *Nat. Rev. Mater.*, 2025, **10**, 566–583.

29 A. Golov, J. X. Lian and J. Carrasco, *ACS Appl. Mater. Interphases*, 2024, **16**, 57870–57877.

30 Q. Wang, Y. Zhou, X. Wang, H. Guo, S. Gong, Z. Yao, F. Wu, J. Wang, S. Ganapathy, X. Bai, B. Li, C. Zhao, J. Janek and M. Wagemaker, *Nat. Commun.*, 2024, **15**, 1050.

31 Y. A. Zulueta and M. T. Nguyen, *Annual Reports in Computational Chemistry*, Elsevier, 2023, vol. 19, pp. 1–43.

32 L. Xia, H. Liu and Y. Pei, *Nanoscale*, 2024, **16**, 15481–15501.

33 Y. A. Zulueta, M. P. Pham-Ho and M. T. Nguyen, *RSC Adv.*, 2024, **14**, 21644–21652.

34 H. Y. Tan, M. Y. Zhou, Z. Huang, J. Da Luo, J. T. Yang, J. P. Wang, Y. C. Wu, X. Bin Cheng, Z. W. Wang, X. D. Hao, L. Wang, K. Gong, Y. C. Yin, Y. Xiao and H. Bin Yao, *Nano Res.*, 2024, **17**, 8826–8833.

35 Y. A. Zulueta, M. T. Nguyen and M. P. Pham-Ho, *RSC Adv.*, 2024, **14**, 22974–22980.

36 L. Huang, L. Zhang, J. Bi, T. Liu, Y. Zhang, C. Liu, J. Cui, Y. Su, B. Wu and F. Wu, *Energy Mater. Adv.*, 2024, **4**, 1–21.

37 X. Nie, J. Hu and C. Li, *Interdiscip. Mater.*, 2023, **2**, 365–389.

38 T. Dai, X. Kouoi, M. Reynaud, M. Wagemaker, M. Valldor, T. Famprikis and A. Y. Koposov, *Energy Storage Mater.*, 2024, **68**, 103363.

39 S. Adams, *Solid State Ionics*, 2006, **177**, 1625–1630.

40 S. Adams and R. P. Rao, *Phys. Chem. Chem. Phys.*, 2009, **11**, 3210–3216.

41 I. D. Brown, *Chem. Rev.*, 2009, **109**, 6858–6919.

42 H. Chen, L. L. Wong and S. Adams, *Acta Crystallogr., Sect. B: Struct. Sci., Cryst. Eng. Mater.*, 2019, **75**, 18–33.

43 Y. A. Zulueta, D.-Q. T. Nguyen, M.-P. Pham-Ho and M. T. Nguyen, *Phys. Chem. Chem. Phys.*, 2025, **27**, 21195–21204.

44 Y. A. Zulueta, N. A. V. Goris, J. R. Fernandez-Gamboa, D. T. Truong, C. M. Phan and M. T. Nguyen, *New J. Chem.*, 2026, **208**, 113194.

45 A. Missoum, M. Mokhtari and F. Dahmane, *Chinese J. Phys.*, 2024, **89**, 1930–1946.

46 K. Bhat, V. Ravathi and V. Srivastava, *Chem. Africa*, 2026, **9**, 3.

47 J. Spector, G. Villeneuve, L. Hanebali and C. Cros, *Mater. Lett.*, 1982, **1**, 43–48.

48 M. C. Payne, M. P. Teter, D. C. Allan, T. A. Arias and J. D. Joannopoulos, *Rev. Mod. Phys.*, 1992, **64**, 1045–1097.

49 D. Vanderbilt, *Phys. Rev. B:Condens. Matter Mater. Phys.*, 1990, **41**, 7892–7895.

50 H. J. Monkhorst and J. D. Pack, *Phys. Rev. B*, 1976, **13**, 5188–5192.

51 J. D. Gale and A. L. Rohl, *Mol. Simul.*, 2003, **29**, 291–341.

52 Computational Modelling of Zinc Oxide and Related Oxide Ceramics - University of Surrey, https://openresearch.surrey.ac.uk/esploro/outputs/doctoral/Computational-Modelling-of-Zinc-Oxide-and/99512944702346, (accessed 21 June 2025).

53 B. A. Goldmann, M. J. Clarke, J. A. Dawson and M. S. Islam, *J. Mater. Chem. A*, 2022, **10**, 2249–2255.

54 B. G. Dick and A. W. Overhauser, *Phys. Rev.*, 1958, **112**, 90–103.

55 N. F. Mott and M. J. Littleton, *Trans. Faraday Soc.*, 1938, **34**, 485–499.

56 J. D. Gale, *J. Chem. Soc., Faraday Trans.*, 1997, **93**, 629–637.

57 F. A. Kröger, *The Chemistry of Imperfect Crystals*, North-Holland Pub. Co, (1964).

58 L. L. Wong, K. C. Phuah, R. Dai, H. Chen, W. S. Chew and S. Adams, *Chem. Mater.*, 2021, **33**, 625–641.

59 C. J. J. Loon and D. J. W. Ijdo, *Acta Crystallogr., Sect. B: Struct. Crystallogr. Cryst. Chem.*, 1975, **31**, 770–773.

60 Data retrieved from the Materials Project for NaMgCl3 (mp-3346580) from database version v2026.01.10. https://next-gen.materialsproject.org/materials/mp-3346580? chemsys = Na-Mg-Cl.

61 M. Born, K. Huang and M. Lax, *Am. J. Phys.*, 1955, **23**, 474.

62 I. N. Frantsevich, F. F. Voronov and S. A. Bokuta, *Elastic Constants and Elastic Moduli of Metals and Insulators Handbook*, Naukova Dumka, Kiev, 1983, pp. 60–180.

63 F. I. Fedorov, *Theory of Elastic Waves in Crystals*, Springer US, Boston, MA, 1968.

64 W. Voigt Lehrbuch der Kristallphysik (BG Teubner Leipzig und 791 Berlin) 980 S; Reproduced 1966 Spring Fachmedien Wiesbaden GmbH, 1928.

65 A. Reuss, *ZAMM - J. Appl. Math. Mech.*, 1929, **9**, 49–58.

66 R. Hill, *J. Mech. Phys. Solids*, 1963, **11**, 357–372.

67 R. Hill, *Proc. Phys. Soc. Sect. A*, 1952, **65**, 349–354.

68 S. I. Ranganathan and M. Ostoja-Starzewski, *Phys. Rev. Lett.*, 2008, **101**, 055504.

69 L. Kleinman, *Phys. Rev.*, 1962, **128**, 2614–2621.

70 R. Ahmed, M. Mahamudujjaman, M. A. Afzal, M. S. Islam, R. S. Islam and S. H. Naqib, *J. Mater. Res. Technol.*, 2023, **24**, 4808–4832.

71 M. Illbeigi, A. Fazlali, M. Kazazi and A. H. Mohammadi, *Solid State Ionics*, 2016, **289**, 180–187.

72 S. F. Pugh, *London, Edinburgh, Dublin Philos. Mag. J. Sci.*, 1954, **45**, 823–843.

73 S. J. Hussain, J. Liu, P.-H. Du, Q. Sun and P. Jena, *ACS Mater. Lett.*, 2025, **7**, 761–769.

74 M. Wu, B. Xu, W. Luo, B. Sun, J. Shi and C. Ouyang, *Appl. Surf. Sci.*, 2020, **510**, 145394.

75 X. Luo, Y. Li and X. Zhao, *Energy Environ. Mater.*, 2024, **7**, e12627.

76 W. Liu, X. Liu, W. T. Zheng and Q. Jiang, *Surf. Sci.*, 2006, **600**, 257–264.

77 Z. Gao, J. Yang, G. Li, T. Ferber, J. Feng, Y. Li, H. Fu, W. Jaegermann, C. W. Monroe and Y. Huang, *Adv. Energy Mater.*, 2022, **12**, 2103607.